

Technical Memo

870

Skin temperature analysis for the assimilation of clear-sky satellite radiances

S. Massart, N. Bormann, M. Bonavita, C. Lupu

August 2020

Series: ECMWF technical memoranda

A full list of ECMWF Publications can be found on our web site under:

<http://www.ecmwf.int/en/publications/>

Contact: library@ecmwf.int

© Copyright 2020

European Centre for Medium Range Weather Forecasts, Shinfield Park, Reading, RG2 9AX, UK

Literary and scientific copyrights belong to ECMWF and are reserved in all countries. This publication is not to be reprinted or translated in whole or in part without the written permission of the Director-General. Appropriate non-commercial use will normally be granted under the condition that reference is made to ECMWF.

The information within this publication is given in good faith and considered to be true, but ECMWF accepts no liability for error, omission and for loss or damage arising from its use.

Summary

Radiances represent the vast majority in numbers of the data that are currently assimilated in the four dimensional variational data assimilation (4D-Var) system of the European Centre for Medium-Range Weather Forecasts (ECMWF) Integrated Forecasting System (IFS). The assimilation of radiances starts with the computation of brightness temperatures expected from the instruments with a radiative transfer code using outputs from the forecast model. These outputs are atmospheric model profiles (e.g., pressure, temperature, specific humidity) and surface parameters (e.g., skin temperature, surface pressure). To produce an optimal model surface and atmospheric state from which the simulated brightness temperatures are the best possible fit to the observed ones, the 4D-Var should be able to optimise the skin temperature together with all the other atmospheric model physical variables.

The control variable of the atmospheric analysis currently does not include surface variables, and the optimisation of the skin temperature is currently achieved by adding a skin temperature component in the 4D-Var control vector, but defined in observation space, i.e., at each observation time and location. This means that for each field of view, if needed, all the observed radiances from this field of view help adjusting a single value of skin temperature, and the optimal skin temperature value is valid only for this field of view. The adjustment is independent of the skin temperature adjustment from other fields of view. In other words, this is a zero-dimensional variational retrieval of the skin temperature at the observation location and time.

A new approach is proposed here where the skin temperature is analysed in model space. The computation of simulated radiances uses the same two-dimensional skin temperature field for all fields of view by interpolating this two-dimensional field at the observation location and time. As a consequence, the combined radiance measurements contribute to the estimation of the skin temperature field in the analysis. This makes the analysed skin temperature field consistent with all available radiance measurements.

The radiative transfer code used in the IFS to compute the radiance equivalent to observation from the model variables admits two separate spectral bands (microwave and infrared) and two different viewing geometries (geostationary and polar) for the infrared band. Sounders from different spectral bands have a different sensitivity to the skin temperature. For example, microwave sounders can penetrate more deeply into the ground layers than the infrared sounders. For this reason, we propose to have a separate skin temperature field per spectral bands (microwave and infrared). For the infrared, we also decided to separate the two viewing geometries as used in the radiative transfer code. The three separate skin temperature fields are referred to as microwave, geostationary (infrared) and (polar, hyper-spectral) infrared.

Having skin temperature fields defined at the beginning of the assimilation window and valid throughout the 12-hour window is not appropriate as the skin temperature as seen by the satellite instruments changes over time within the window, especially over land. At this stage, we do not know how to evolve in time these skin temperature fields. We have instead chosen to extend the skin temperature control vector with one skin temperature field per hour, i.e., 13 fields over the 12-hour assimilation window length, per instrument type.

This paper describes the technical and scientific developments connected to this new skin temperature analysis. In particular, we focus on the background errors of the new skin temperature fields that are introduced to the control vector. With sensitivity studies, we found some configurations of the new approach for which the skin temperature analysis for the radiance assimilation is similar to the current formulation. These configurations also produce similar analysis fit to observations than the current formulation except for particular channels sensitive to the surface. Yet, the first guess fit to observation is not significantly different between them.

The new approach has a neutral impact on the analysis and a neutral to positive impact on the forecast scores. This is encouraging as there is room for improvement. Moreover, the analysed skin temperature fields are by-products that could help future developments of the skin temperature model or future developments of the radiance observation operator.

1 Introduction

Radiances represent the vast majority in numbers of the data that are currently assimilated in the four dimensional variational data assimilation (4D-Var) system of the European Centre for Medium-Range Weather Forecasts (ECMWF) Integrated Forecasting System (IFS). Although other satellite measurements make important contributions to the ECMWF forecasting skill, microwave and infrared soundings are among the most important contributors when it comes to improve the forecast skill (McNally, 2015).

The 4D-Var method for a given time window is based on all observations available during this window, on a background model state valid at the initial time of the window, and also on the specification of observation and background errors (Rabier *et al.*, 2000). It then provides the analysis, an optimal model state that simultaneously minimises the model state distance from the background and from the observations, accounting for the respective errors. The model-observations distance relies on the difference between each observation and the model state at the observation time obtained by first integrating in time the model state defined at the initial time. The model state at the appropriate observation time is then transformed into an observation-equivalent by the so-called observation operator.

For radiance assimilation, the observation operator contains a radiative transfer component that integrates the radiative transfer equation from the outputs of the forecast model along the viewing path. This requires model profiles of pressure, temperature, specific humidity, cloud properties and atmospheric composition, and, for the surface, surface emissivity, skin temperature, surface pressure, 2m-temperature, 2m-humidity and 10m-wind. The sensitivity to the various layers of the atmosphere and to the surface in the radiative transfer equation depends on the frequency of the measurement. Observing radiances at various frequencies therefore provide indirect information on the atmospheric variables on diverse atmospheric layers and on the surface variables. Indeed, the assimilation of a radiance observation at a specific frequency works by adjusting the model atmospheric variables mostly around the model levels where the observed radiance has its largest sensitivity (peak of its weighting function, Rodgers, 2000) and by adjusting the model surface variables if there is some sensitivity to the surface. The adjustment is such that the changes in the model variables produces a simulated radiance that is as close to the observed radiance as possible and consistent with the assumed uncertainties on the background state and on the observation.

In the IFS, the atmospheric analysis and the surface analysis are only coupled during the first guess forecast step, not during the analysis update itself (weak coupling, de Rosnay *et al.*, 2014; Browne *et al.*, 2019). Hence, assimilating radiances for the atmospheric analysis at frequencies sensitive to the surface variables without consistently adjusting surface variables is problematic. An inaccurate emissivity or skin temperature from the model could lead to an inaccurate analysis of the temperature profile for example. To bypass this issue, the spectral channels currently entering the atmospheric analysis are carefully selected to avoid those which are very sensitive to the surface, and at the same time to keep those which have a significant positive forecast impact in the ECMWF system (Bormann *et al.*, 2017). Over ocean, the required surface emissivity is modeled using appropriate fast parameterised models (English *et al.*, 1998; Kazumori *et al.*, 2015). Over land or sea-ice, where surface emissivity models are currently less accurate, atlas values are used in the case of infrared observations, whereas surface emissivity is retrieved from window channels for microwave observations (Karbou *et al.*, 2006). In the latter case, model background values are used in the emissivity inversion, including that of the model skin temperature.

The inclusion of the skin temperature in the control vector of the atmospheric analysis was developed in the early 90's at ECMWF when the radiances from the TOVS (TIROS-N (Television Infra-Red Observation Satellite) Operational Vertical Sounder) sounder were directly assimilated (Eyre *et al.*, 1992). Since

then, this technique is referred to as TOVS Control Variable (TOVSCV, [ECMWF, 2019](#)) and it is used in the assimilation of clear-sky radiances. All the radiances associated with a particular field of view of a given instrument share the same value of skin temperature in the radiative transfer code used in the IFS. This gives a value of skin temperature per field of view per instrument. The TOVSCV approach consists in adding all these separate values of skin temperature to the control vector. Then, the individual skin temperatures are optimised in the 4D-Var minimisation together with the other model physical variables to produce an optimal model state from which the simulated radiances are the best possible fit to the observed radiances.

When assimilating a group of radiances within the same field of view, the model state along the viewing path is constrained by these radiance observations, but also by all the other measurements available within a volume centred around the field of view and with a size proportional to the background error local decorrelation lengths. By contrast, in the TOVSCV approach the skin temperature is only constrained by the radiances within the same field of view and therefore is free to be adjusted within the constraint of its background error and within the constraint of the sensitivity of each radiance frequency to the skin temperature. Because of this lack of constraint by other surrounding measurements, it is likely that the skin temperature adjustment compensates for other errors in the background state, thus reducing the optimality of the analysis.

A new approach is proposed here, where the skin temperature adjustment takes place in model space. The computation of simulated radiances with the radiative transfer code uses the same two-dimensional skin temperature field for all fields of view by interpolating this two-dimensional field at the observation location. As a result, in the analysis, all the radiance observations for which the field of view is included in the volume defined by the background error local decorrelation lengths contribute to the estimation of the skin temperature field in a more physically consistent way. We want to assess if this additional constraint on the skin temperature can improve the use of satellite radiance data in the IFS analysis. First, we present in more details the radiance assimilation and the two approaches for the optimisation of the skin temperature used in the radiance observation operator. Then, we detail the possible choices for the background errors of the skin temperature fields introduced to the control vector in the new approach and we present the first results obtained with a simple configuration of the background errors. Finally we present a sensitivity study to the choices of the background errors before concluding on the future work.

2 Skin temperature in the assimilation of radiance

In this section, we describe how the skin temperature is included in the observation operator used in the IFS to assimilate radiances for the atmospheric analysis. We then present how the skin temperature is currently included in the control vector and optimised in observation space. We finally present the novel approach that adds a skin temperature field in model space to the control vector to make the skin temperature analysis consistent (in time and space) between all radiance measurements. We focus here only on the assimilation of the radiance measurements sensitive to the surface. We ignore for simplicity all the other type of measurements that are operationally assimilated in the IFS.

2.1 Radiance assimilation

Let us introduce y_i^o , an observed set of radiances at various frequencies but all belonging to the same field of view and measured by the same instrument, and for which i is the index of the observation in the observation vector y^o . To assimilate these observed radiances, one has to first compare them to

equivalent radiances derived from the model variables (or simulated radiances). These model-equivalent radiances are obtained with the observation operator H_i applied to the model state vector \mathbf{x}_i at the time of the observation,

$$\mathbf{y}_i = H_i(\mathbf{x}_i). \quad (1)$$

The model state vector contains the three-dimensional distribution of the atmospheric model variables and the two-dimensional distribution of the surface model variable at the observation time. In practice, the part of the observation operator that integrates the radiative transfer equation requires only the profile of the atmospheric model variable along the viewing path and the surface variables at the observation location. The observation operator H_i is then decomposed into the combination of two operators: (i) $H_{I,i}$ that performs the interpolation of the state vector \mathbf{x}_i to produce profiles of the model variables along the viewing path and values of the model surface variables at the observation location, and (ii) $H_{R,i}$ that performs the radiative transfer computation to convert the interpolated model state into radiance at the required frequencies. In the IFS, this operation is performed by the Radiative Transfer for TOVS (RT-TOV, [Matricardi et al., 2004](#); [Saunders et al., 2018](#)) code. Using this decomposition of the observation operator, the model equivalent to a radiance is expressed as

$$\mathbf{y}_i = H_{R,i} \circ H_{I,i}(\mathbf{x}_i). \quad (2)$$

Let us explicitly introduce τ_i , the skin temperature at the observation location, into the observation operator equation,

$$\mathbf{y}_i = H_{R,i}(H_{I,i}(\mathbf{x}_i), \tau_i). \quad (3)$$

In practice, the skin temperature τ_i used in the observation operator is the skin temperature from the first guess extracted at the observation time and interpolated in space using $H_{I,i}$. The model state at the observation time \mathbf{x}_i comes from the model state at initial time \mathbf{x}_0 and integrated by the model $\mathcal{M}_{i,0}$ between the initial time and the time of the observation \mathbf{y}_i^o ,

$$\mathbf{x}_i = \mathcal{M}_{i,0}(\mathbf{x}_0), \quad (4)$$

2.2 Current formulation of TOVSCV

The idea behind the TOVSCV approach is to adjust τ_i together with the atmospheric variables. With this aim, each τ_i is renamed $x_{p,i}$ and the observation operator equation becomes

$$\mathbf{y}_i = H_{R,i}(H_{I,i}(\mathbf{x}_i), x_{p,i}). \quad (5)$$

All the scalar values $x_{p,i}$ are concatenated into the vector \mathbf{x}_p . It is added to the atmospheric control vector \mathbf{x}_0 containing the atmospheric variables at initial time. The combination of both vector leads to the augmented control vector

$$\tilde{\mathbf{x}} = \begin{pmatrix} \mathbf{x}_0 \\ \mathbf{x}_p \end{pmatrix}. \quad (6)$$

There are fundamental differences between these two components. First, \mathbf{x}_0 is a vector containing the atmospheric model variables defined on the model grid and at initial time. On the other hand, \mathbf{x}_p is a vector containing a surface variable at the observation locations and at the observation time. For these reasons we identify \mathbf{x}_p as defined in observation space while \mathbf{x}_0 is defined in model state and at initial time.

With the form of Eq.(6) for the control vector, it is clear that both components are optimised simultaneously. The part of the cost function related to the radiance observations is then

$$J^o(\mathbf{x}_0, \mathbf{x}_p) = \frac{1}{2} \sum_i [\mathbf{y}_i^o - H_{R,i}(H_{I,i}(\mathbf{x}_i), x_{p,i})]^T \mathbf{R}_i^{-1} [\mathbf{y}_i^o - H_{R,i}(H_{I,i}(\mathbf{x}_i), x_{p,i})], \quad (7)$$

where \mathbf{R}_i^{-1} is the observation error covariance matrix for the observation \mathbf{y}_i^o . From this equation, we can compute the gradient of the part of the cost function related to the radiance observations with respect to each component $x_{p,i}$ of the vector \mathbf{x}_p ,

$$\frac{\partial J^o(\mathbf{x}_0, \mathbf{x}_p)}{\partial x_{p,i}} = \mathbf{H}_{R,i}^T \mathbf{R}_i^{-1} [\mathbf{y}_i^o - H_{R,i}(H_{I,i}(\mathbf{x}_i), x_{p,i})], \quad (8)$$

where $\mathbf{H}_{R,i}^T$ is the adjoint of $H_{R,i}$ with respect to $x_{p,i}$. It is clear from this expression that the only observations that will directly contribute to the update of $x_{p,i}$ are \mathbf{y}_i^o , i.e. all the radiances within the same field of view of the same instrument.

The background part of the cost function should also account for the fact that the control vector is augmented with \mathbf{x}_p . Currently, the background errors between the model state vector \mathbf{x}_0 and the interpolated skin temperatures in observation space \mathbf{x}_p are assumed to be uncorrelated. If \mathbf{B} is the error covariance matrix associated with the background state \mathbf{x}_0^b of \mathbf{x}_0 and \mathbf{B}_p is the error covariance matrix associated with the background state \mathbf{x}_p^b of \mathbf{x}_p , then the background part of the cost function is

$$J^b(\mathbf{x}_0, \mathbf{x}_p) = \frac{1}{2} [\mathbf{x}_0 - \mathbf{x}_0^b]^T \mathbf{B}^{-1} [\mathbf{x}_0 - \mathbf{x}_0^b] + \frac{1}{2} [\mathbf{x}_p - \mathbf{x}_p^b]^T \mathbf{B}_p^{-1} [\mathbf{x}_p - \mathbf{x}_p^b]. \quad (9)$$

The background state \mathbf{x}_p^b is derived from the background values of the skin temperature,

$$x_{p,i}^b = \tau_i. \quad (10)$$

The background error covariance matrix \mathbf{B}_p associated with \mathbf{x}_p is currently diagonal (with different values over the diagonal for different surface types, i.e., land, sea, sea-ice). This means that the observation \mathbf{y}_i^o will bring information on $x_{p,i}$ as shown by Eq.(8), and only on $x_{p,i}$ because of the lack of cross-covariances in \mathbf{B}_p . There is thus no spatial consistency among the analysed values of the skin temperatures $x_{p,i}$ in observation space and each value $x_{p,i}$ is analysed independently from each other.

The minimisation of the 4D-Var cost function in the IFS follows the incremental approach proposed by [Courtier *et al.* \(1994\)](#). This is an iterative process in which the 4D-Var cost function is successively linearised around a first guess. The first guess is chosen as the analysis from the previous iteration or the background state for the first iteration. The TOVSCV implementation follows the incremental approach and a new first guess of \mathbf{x}_p^s is computed at every outer loop iteration. The iterative process also provides a new first guess of the skin temperature from the model, but this is currently not used for the radiance assimilation.

To summarise the TOVSCV approach, the assimilation of a set of radiance observations from the same field of view \mathbf{y}_i^o will adjust locally the three-dimensional atmospheric variables and the local skin temperatures $x_{p,i}$ to provide simulated radiances that fit in an optimal manner \mathbf{y}_i^o according to the prescribed observations and the background errors. The atmospheric variables are also constrained by surrounding observations while $x_{p,i}$ is not. Therefore we refer to this approach as TOVSCV_0D in the rest of this document.

Currently, in the IFS, the radiance observations are thinned to a resolution of around 125 km and concatenated into 30 min time slots. Over land, the skin temperature can be spatially very heterogeneous and

can change quickly in time. Under these conditions, and if the characteristic length scale of the spatial heterogeneity is lower than 125 km and the characteristic time scale is under 30 min, the TOVSCV_0D approach could be sufficient. For other situations that may occur over ocean where the skin temperature is more homogeneous and varies slowly in time, we believe that the TOVSCV_0D approach could be improved by constraining $x_{p,i}$ with surrounding radiance observations. We expect that this additional constraint could be beneficial for the assimilation of the radiance observations.

2.3 New formulation

It would be possible to constrain neighbouring values of \mathbf{x}_p in the current TOVSCV_0D formulation by adding correlations in the associated background errors. But this would require to build a correlation model in space and in time on the unstructured grid formed by the current set of observation locations and times. We propose instead a new formulation for TOVSCV that analyses the skin temperature used in the radiative transfer equation directly in model space.

2.3.1 Skin temperature analysis in model space

The new formulation is also based on Eq. (3), but the skin temperature value τ_i is replaced by a two-dimensional field concatenated into the vector \mathbf{x}_α and interpolated to the observation location. We choose this field to have the same horizontal dimension as \mathbf{x}_0 and we use the same interpolation operator $H_{I,i}$, so τ_i becomes $H_{I,i}(\mathbf{x}_\alpha)$ and Eq.(3) becomes

$$\begin{aligned} \mathbf{y}_i &= H_{R,i}(H_{I,i}(\mathbf{x}_i)H_{I,i}(\mathbf{x}_\alpha)) \\ &= H_{R,i} \circ H_{I,i}(\mathbf{x}_i, \mathbf{x}_\alpha). \end{aligned} \quad (11)$$

As in the previous method, the vector \mathbf{x}_α is added to the control vector \mathbf{x} to form the augmented control vector

$$\tilde{\mathbf{x}} = \begin{pmatrix} \mathbf{x}_0 \\ \mathbf{x}_\alpha \end{pmatrix}. \quad (12)$$

Now, the part of the cost function related to the radiance observations is

$$J^o(\mathbf{x}_0, \mathbf{x}_\alpha) = \frac{1}{2} \sum_i [\mathbf{y}_i^o - H_{R,i} \circ H_{I,i}(\mathbf{x}_0, \mathbf{x}_\alpha)]^T \mathbf{R}_i^{-1} [\mathbf{y}_i^o - H_{R,i} \circ H_{I,i}(\mathbf{x}_0, \mathbf{x}_\alpha)], \quad (13)$$

and its gradient with respect to \mathbf{x}_α is

$$\frac{\partial J^o(\mathbf{x}_0, \mathbf{x}_\alpha)}{\partial \mathbf{x}_\alpha} = \sum_i \mathbf{H}_{I,i}^T \mathbf{H}_{R,i}^T \mathbf{R}_i^{-1} [\mathbf{y}_i^o - H_{R,i} \circ H_{I,i}(\mathbf{x}_0, \mathbf{x}_\alpha)], \quad (14)$$

where $\mathbf{H}_{I,i}^T$ is the adjoint of $H_{I,i}$ with respect to \mathbf{x}_α . From these expressions of the part of the cost function related to the radiance observations and its gradient, it is clear that all radiance observations will contribute to optimise the vector \mathbf{x}_α . The information from the observation space toward the model space is propagated through $\mathbf{H}_{I,i}^T$. If, for example, $H_{I,i}$ is a bi-linear interpolation then $\mathbf{H}_{I,i}^T$ will propagate back the information in the four surrounding model grid cells of the observation location. All other radiance observations for which the field of view is within these grid cells will also provide information on the skin

temperature of these grid cells. The information is then further spread in space through the background error covariances \mathbf{B}_α associated with \mathbf{x}_α and present in the background part of the cost function

$$J^b(\mathbf{x}_0, \mathbf{x}_\alpha) = \frac{1}{2} [\mathbf{x}_0 - \mathbf{x}_0^b]^T \mathbf{B}^{-1} [\mathbf{x}_0 - \mathbf{x}_0^b] + \frac{1}{2} [\mathbf{x}_\alpha - \mathbf{x}_\alpha^b]^T \mathbf{B}_\alpha^{-1} [\mathbf{x}_\alpha - \mathbf{x}_\alpha^b]. \quad (15)$$

The expressions of Eq.(15) for the background term of the cost function is derived under the assumption that the newly introduced background of the skin temperature \mathbf{x}_α^b is bias-free. This might be a strong assumption in our context where the background value is the model skin temperature while \mathbf{x}_α represents a skin temperature as used in the radiative transfer equation and whose depth depends on the simulated radiance frequency. On the other hand, we do not have a prior knowledge on the potential bias of the skin temperature field \mathbf{x}_α . As a first step we neglect it, but if needed the cost function could account for such biases as it can account for biases in the forecast model (Trémolet, 2006).

Similarly, the expressions of Eq.(13) for the observation term of the cost function does not account for observation biases. In practice, observational biases are addressed through the Variational Bias Correction (VARBC, Dee, 2004). VARBC can be used together with the new TOVSCV approach without requiring any specific modification.

The incremental formulation of IFS 4D-Var produces a first guess for \mathbf{x}_α at each iteration. This first guess is used to linearise the observation operator in Eq. (11). Note that, in parallel, the surface analysis also produces a new first guess for the skin temperature. This new first guess from the surface analysis is currently disregarded in the observation operator for the radiance assimilation.

The forecast model integrates in time the 4D-Var analysis state to produce the background for the next cycle. Here, we do not propagate in time the analysis of \mathbf{x}_α . Instead, we use the background skin temperature as the new background \mathbf{x}_α^b for the next assimilation cycle.

To summarise, we have introduced a new variable \mathbf{x}_α in the 4D-Var control vector that is a two-dimensional field in the model space representing the skin temperature. This field is used in the observation operator for the clear-sky radiance assimilation instead of the discrete values of the current TOVSCV_0D approach. We refer to the new approach as TOVSCV_2D. In this new approach, the transformation of model variables into equivalent to radiance observations is based on the same skin temperature field for all observations and, as a consequence, all radiance observations are used to optimise this field.

The initial results obtained with this new formulation were encouraging but we encountered a degradation of the analysis fit to observation for some satellite instruments using this field. We traced back this degradation to two plausible causes. First, the skin temperature may not have the same meaning for different instruments as the depth of the surface layer that contributes to the observed radiation depends on the used spectral band. Secondly, in the initial setup of the TOVSCV_2D experimentation, we were not accounting for the time evolution of the skin temperature by having a single field valid for the entire assimilation window. These two issues are addressed in the next two sections.

2.3.2 Decomposition by satellite instrument type

The ground depth down to which a radiance observation is sensitive to depends on the frequency of its measurement (Prigent *et al.*, 1999). This depth defines the skin temperature for this particular radiance observation, which makes the skin temperature dependent on the spectral band of the observation. For this reason, we decided that it would be better to have a different skin temperature field per spectral bands.

The radiative transfer code RTTOV used in the observation operator makes a distinction between two separate spectral bands (microwave and infrared) and uses two different viewing geometries (geostationary and polar) for the infrared band. This makes three distinct categories for the radiance measurements referred to hereafter as: microwave (*mw*), geostationary infrared (*ir*), and hyper-spectral infrared (*hi*). We decided as a first improvement, to use the same three categories in the new formulation by introducing three separate two-dimensional fields in \mathbf{x}_α instead of one,

$$\mathbf{x}_\alpha = \begin{pmatrix} \mathbf{x}_\alpha^{mw} \\ \mathbf{x}_\alpha^{ir} \\ \mathbf{x}_\alpha^{hi} \end{pmatrix}. \quad (16)$$

The geostationary and hyper-spectral infrared instruments have similar observation wavelengths and should share the same skin temperature field. Here, we decided to separate the two viewing geometries mainly to follow the RTTOV implementation, and not because we expected a difference from the viewing geometry. On the other hand, as detailed in section 4, the selected radiance observations from the geostationary infrared instruments should not be sensitive to the surface. Having a dedicated field for them should help assessing if, in our system, the assimilation of radiance observations from geostationary infrared instruments is sensitive to the skin temperature.

The background error covariances and the observation operator account for the introduction of three fields. First, we assume in the following that there is no cross-correlation in the background errors of the skin temperature fields between the three previously defined types. This is a strong assumption, especially for the two infrared fields, but it reflects that we have at this stage little knowledge of these cross-correlations. The background error covariance matrix is then block-diagonal, each block representing a type,

$$\mathbf{B}_\alpha = \begin{pmatrix} \mathbf{B}_\alpha^{mw} & \mathbf{0} & \mathbf{0} \\ \mathbf{0} & \mathbf{B}_\alpha^{ir} & \mathbf{0} \\ \mathbf{0} & \mathbf{0} & \mathbf{B}_\alpha^{hi} \end{pmatrix}. \quad (17)$$

The observation operator then introduces a selection operator $H_{S,i}$ before the interpolation,

$$H_{S,i} = \begin{pmatrix} H_{S,i}^{mw} & H_{S,i}^{ir} & H_{S,i}^{hi} \end{pmatrix}. \quad (18)$$

where, for example, $H_{S,i}^{mw}$ is equal to identity for a microwave measurement and zero otherwise. The model equivalent to a radiance observation is then

$$\mathbf{y}_i = H_{R,i} \circ H_{I,i}(\mathbf{x}_i, H_{S,i}(\mathbf{x}_\alpha)). \quad (19)$$

2.3.3 Time dependent skin temperature

Over land, the amplitude of the skin temperature diurnal cycle can be considerable. Over desert areas, the difference between the minimum and maximum skin temperature during the day can reach 30 K (Pinker *et al.*, 2007). Over ocean, the amplitude of the surface temperature diurnal cycle is usually small and less than 1 K. Nevertheless, the amplitude can be larger during particular events. For example, daily increases between 5 K and 7 K were observed by independent satellite measurements of ocean surface temperature (Gentemann *et al.*, 2008). For these reasons, the fields in \mathbf{x}_α should also evolve in time within the 12-hour assimilation window.

To propagate in time \mathbf{x}_α , one could use the equations of the forecast model that propagate in time the skin temperature. But, as already discussed in the previous subsection, the meaning of skin temperature is different between instrument types and therefore different from the model skin temperature. At this stage, we do not know if the equations from the forecast model are relevant or not for any/all of the fields in \mathbf{x}_α .

Our strategy is to instead expand the control vector \mathbf{x}_α to one skin temperature field per hour and per instrument. For a 12-hour assimilation window, we then have 13 fields per instrument.

$$\mathbf{x}_\alpha^{mw} = \begin{pmatrix} \mathbf{x}_\alpha^{mw}(t_0) \\ \vdots \\ \mathbf{x}_\alpha^{mw}(t_{12}) \end{pmatrix}, \quad \mathbf{x}_\alpha^{ir} = \begin{pmatrix} \mathbf{x}_\alpha^{ir}(t_0) \\ \vdots \\ \mathbf{x}_\alpha^{ir}(t_{12}) \end{pmatrix}, \quad \mathbf{x}_\alpha^{hi} = \begin{pmatrix} \mathbf{x}_\alpha^{hi}(t_0) \\ \vdots \\ \mathbf{x}_\alpha^{hi}(t_{12}) \end{pmatrix}. \quad (20)$$

This means that now \mathbf{x}_α contains $3 \times 13 = 39$ two-dimensional fields. We then introduced a time selection operator in the radiance observation operator together the instrument selector $H_{S,i}$. For each observation, the time selection operator selects from \mathbf{x}_α the two closest fields in time from the observation time, for the relevant instrument. Then, it performs a linear interpolation in time between these two fields.

Again, at this stage, we do not have any prior knowledge on how the three vectors \mathbf{x}_α^{mw} , \mathbf{x}_α^{ir} , \mathbf{x}_α^{hi} differ and we choose to use the same background for them all. This background is the concatenation of the hourly fields of skin temperature from the short-range forecast.

We allow for each instrument type to have correlation in the background errors between the fields at different times. This is implemented by keeping the same block-diagonal shape as in Eq. (17) for the background error covariance matrix \mathbf{B}_α , but with each block containing the time-covariances between the fields of a same instrument.

In absence of a model to propagate in time the fields in \mathbf{x}_α , our strategy is the closest possible to a 4D-Var. By having hourly analysed skin temperature fields, we expect to be able to learn about the time evolution of these fields and eventually to build a model for their time evolution.

3 Background errors for the TOVSCV_2D formulation

As new components of the control vector, the new fields associated with the skin temperature require the specification of their background error covariance matrix. Similarly to other variables of the control vector, we decompose the background error covariances of the new fields into the background error standard deviations and the background error correlations using the wavelet formulation (Fisher et Andersson, 2001).

Differently to the other variables of the control vector, we have one field per hour (for each instrument). This means that on top of the spatial correlations of the background errors, we also have temporal correlations that we should account for. Note that, at this stage, we do not account for the cross-correlation between the errors of the three instrument categories.

3.1 Standard deviation

The current formulation of TOVSCV_0D already requires values for the standard deviation of the skin temperature background errors. Until IFS Cycle 47R1 we were using fixed values over specific regions

(land, sea and ice) as specified in the first row of Tab. 1, and a linear interpolation was performed at the interface between the regions.

Table 1: Skin temperature background error standard deviation per surface type for the fixed values and as derived from the EDA for the 20191101 09Z cycle. The first value is the global mean and the second value is the spatial standard deviation (for the EDA only).

	Land	Sea	Ice
Fixed	5.00 K	1.00 K	7.50 K
EDA	0.45 ± 0.22 K	0.27 ± 0.10 K	0.55 ± 0.21 K

For the new TOVSCV_2D formulation, we are building the skin temperature background error standard deviation map using the same fixed values as for TOVSCV_0D over specific regions and a linear interpolation at the interface between the regions (Fig. 1a). Similarly to the other variables of the control vector, the standard deviation map is computed on a T159 horizontal resolution grid. For that particular choice of background error standard deviation, we have the same map for each skin temperature field, independently of the instrument type or time.

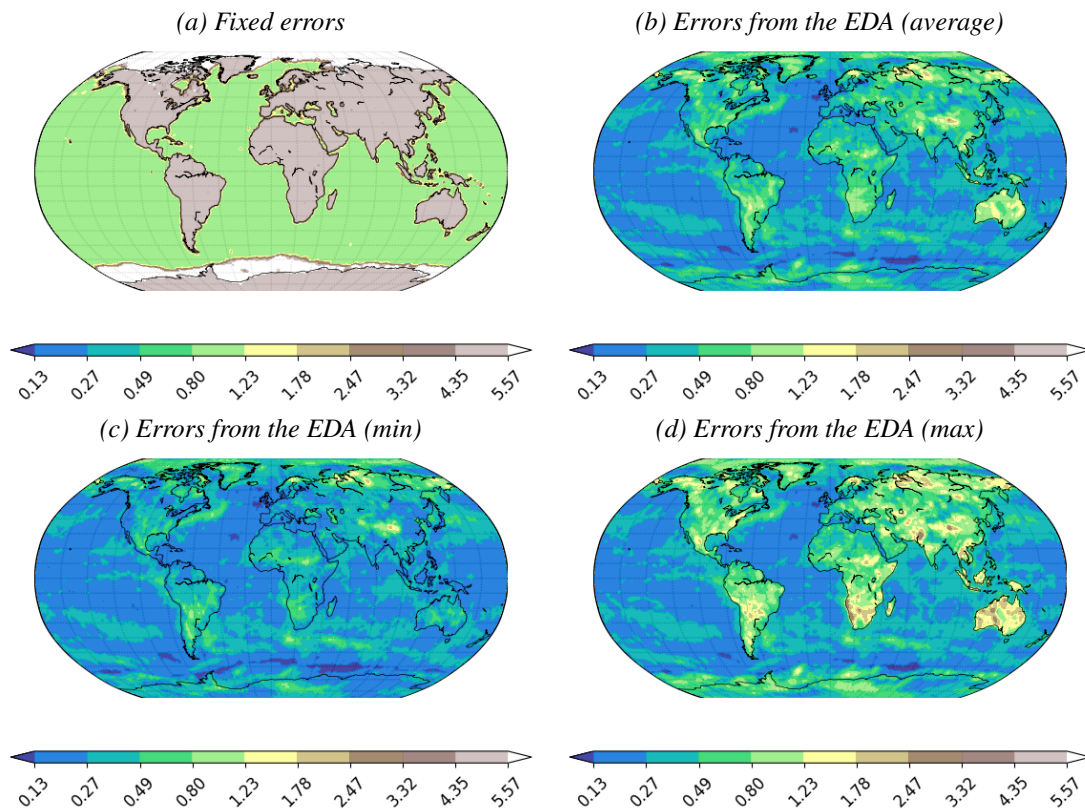


Figure 1: Example of skin temperature background error standard deviation (in K) (a) using fixed values or (b) to (d) as derived from the EDA (average/min/max for the 20191101 09Z cycle).

For most variables of the control vector, the background error standard deviation comes from the ensemble of data assimilations (EDA, Bonavita *et al.*, 2012). The skin temperature background error standard deviation is now estimated hourly as part of the 50-members EDA starting with IFS Cycle 47R1 (Cristina Lupu, ECMWF, personal communication). An example of skin temperature background error standard

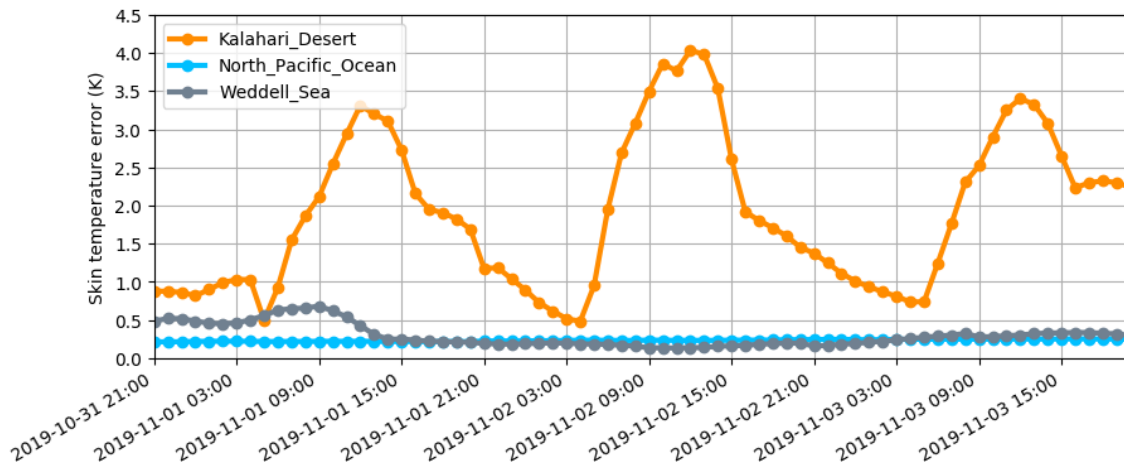


Figure 2: Example of time variation of the skin temperature background error standard deviation (in K) as derived from the EDA for three particular grid points: Kalahari Desert (land, 23°S, 22°E), North Pacific Ocean (sea, 40°N, 140°W), Weddell Sea (ice, 72°S, 36°W).

deviation from the EDA is displayed in Fig. 1. The mean value and spatial standard deviation for the same date are reported in row 2 of Tab. 1.

The skin temperature background error standard deviation derived from the EDA presents some spatial variability over the three types of surface. The EDA is also able to capture the time variability of the skin temperature background error standard deviation as illustrated by Fig. 2. From these three selected locations used as examples, we see a strong diurnal variation for the desert location, little time-variation for the ocean location and longer time-scale variation for the ice location. These features mean that we could expect some impact on analyses of the skin temperature fields using an EDA-derived skin temperature background error standard deviation.

However, the absolute values of the standard deviation from the EDA are on average much smaller than the prescribed ones, by a factor more than 10 over land and ice and by a factor of about 3 over sea. Because of these large differences, using the background error standard deviation from the EDA requires some more tuning. This work is being conducted in the TOVSCV_0D framework and we expect to further benefit from it.

Despite the large differences between the prescribed and the EDA-based background error standard deviations, we have chosen to develop for the TOVSCV_2D formulation the capability to use a background error standard deviation formulation based on the EDA outputs. Then, each hourly skin temperature field has its own background error standard deviation derived from the hourly outputs of the EDA. The standard deviation are assumed the same for all three instrument types.

3.2 Spatial correlation

The first component of the background error correlations is the spatial correlations. We used the Hybrid-Diag software to diagnose the length scales that best fit the local diagnosed spatial correlation using a Gaussian shape (Ménétrier et Auligné, 2015). Using the hourly skin temperature fields from a 50 members EDA, we saw some local variations in time of the optimal length scale. These temporal variations are found to be small compared to the spatial variations. Therefore, as a first step, we decided to build a

static background error correlation model rather than a flow dependent one.

We diagnosed the static background error correlations using EDA forecasts from 10 dates, starting from 1 November 2019 and incrementing the dates by 3 days. For each date, we selected for each of the two 12 h cycles the 50 members at the beginning of the window. The skin temperature background error correlations are thus estimated using 20 sets of 50 members. From the local estimation of the correlation $\rho(\delta\mathbf{x})$ as a function of the local distance $\delta\mathbf{x}$, we search the best local Gaussian length scale L_g that minimises the distance between $\rho(\delta\mathbf{x})$ and

$$\rho_g(\delta\mathbf{x}) = \exp\left(-\frac{\|\delta\mathbf{x}\|^2}{2L_g^2}\right). \quad (21)$$

The diagnosed Gaussian length scale L_g is on average around 300 km, with large spatial variations (Fig.3a). The diagnosed length scale is in average around 118 km over land, around 106 km over ice and around 340 km over sea (Tab. 2). Over ocean, the further from the coast, the larger the length scale. There are nevertheless some large scale structures in the length scale field that seem to follow the main ocean currents with higher values inside the gyres.

Table 2: Statistics of the diagnosed Gaussian length scale L_g per region.

	Land	Sea	Ice
Average	117.76 Km	340.41 Km	106.18 Km
Median	110.20 Km	336.41 Km	105.82 Km
Minimum	60.25 Km	70.81 Km	67.73 Km
Maximum	337.51 Km	689.44 Km	190.92 Km

We should expect a bigger difference between the two TOVSCV formulations over oceans where the length scales are the largest and mostly larger than the data thinning resolution (around 125 Km). Over ice, we should not expect a large difference. Over land, we should expect some regional differences as the length scale varies between about 60 Km and 337 Km.

Small length scales over land and ice reflect a sub-grid variability of the skin temperature. In these situations, the observation operator should include a representativeness error. At this stage, we are not accounting for this additional error.

3.3 Temporal correlation

We proposed to have one field per hour for the skin temperature in the TOVSCV_2D formulation as we do not use a model for its time evolution. We associated a background error standard deviation and spatial correlation for each of these fields. We can also associate a temporal correlation between them. Using the 50 members EDA, we can estimate the local time correlation and also find the optimal Gaussian time scale that best fits the time correlation.

We found again large disparities in the values of the estimated time scale between land/ice and ocean (Fig.3b). Over ocean, the time scale values are mostly over 24 h except in the Western Pacific where they can be shorter than 12 h. Over land, there is a range of values of the time scale mainly between 2 h and 12 h.

When using the diagnosed time scale field in the model of the time correlation for the skin temperature background error, we can expect to resolve the diurnal cycle over land and to have a smooth field in time

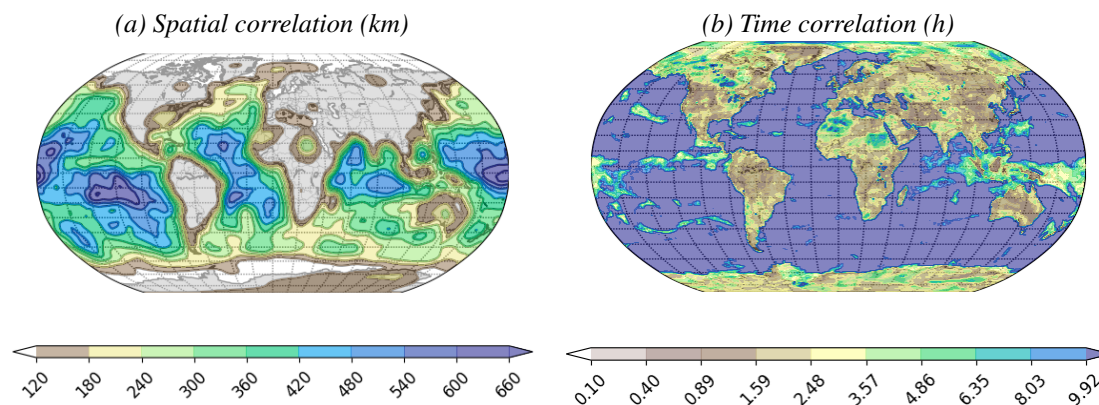


Figure 3: Example of (a) spatial correlation length scale (in km) and (b) temporal correlation length scale (in h) of the skin temperature background error as derived from the EDA.

over ocean.

4 Initial results of the TOVSCV_2D formulation

4.1 Experimentation

To assess the behaviour of the new TOVSCV_2D formulation we ran for the month of November 2019 an experiment using this formulation, using the IFS cycle CY47R1 with RTTOV version 12.2 (Saunders *et al.*, 2018). As a first test of the TOVSCV_2D formulation, we started with a simple configuration as described hereafter. The background error standard deviations are fixed per surface type as reported in the first row of Tab 1. For the background error spatial correlation we are using a constant length scale of 300 km and there is no temporal correlation. We refer hereafter to this experiment as TOVSCV_2D_REF.

In parallel, we ran two other experiments, similar to the previous one apart for the treatment of TOVSCV. In the REFERENCE experiment, we switched off TOVSCV, while in the TOVSCV_0D experiment we switched it on in its current observation space implementation, and we used the same fixed background errors standard deviation for the skin temperature as for the TOVSCV_2D_REF experiment. Note that for all experiments, the cloud sink control variable described in McNally (2009) is disabled as this feature is not yet available together with the TOVSCV_2D formulation.

Table 3 presents a list of instruments providing clear-sky radiance observations and assimilated in the IFS cycle CY47R1. The instruments are presented by category following the three categories defined before for the skin temperature fields. For the microwave category, the AMSU-A instruments have only 50 GHz channels, while ATMS has the additional 183 GHz channels. For the geostationary instruments, the channels the most sensitive to the surface (window channels) are not assimilated and the data over a grid cell where the model orography is higher than 1.5 Km are also rejected. For the hyper-spectral instruments, the list of selected channels is too long to add to the table. Instead, we have added the reference for the channel selection.

Table 3: List of instruments used in clear-sky radiance assimilation in the ECMWF system.

Category	Instrument	Payload	Channel / Waveband
Microwave	AMSU-A	AQUA	Ch 8-14
		METOP-A METOP-B NOAA 15 NOAA 18 NOAA 19	Ch 5-14
	ATMS	NOAA 20 NPP	Ch 6-15 & 18-22
	MWHS	FY-3B	Ch 3-5
Geostationary	IMAGER	GOES 15	6.55 μm
	ABI	GOES 16	6.15 & 7.00 & 7.40 μm
	AHI	Himawari 8	6.25 & 6.95 & 7.35 μm
	SEVIRI	METEOSAT 8	6.25 & 7.35 μm
	SEVIRI	METEOSAT 11	6.25 & 7.35 μm
Hyper-spectral	IASI	METOP-A METOP-B	Collard (2007)
	AIRS	AQUA	Collard (2008)
	CRIS	NOAA 20 NPP	Eresmaa et al. (2017)

4.2 Results in model space

The TOVSCV_2D_REF provides three skin temperature analysis fields per hour as derived by the assimilation of radiance observations from microwave, geostationary infrared and hyper-spectral infrared instruments. To simplify the discussion, we will refer to these three hourly fields as microwave, geostationary and infrared (skin temperature) fields respectively.

From the hourly skin temperature analysis fields, we can subtract the hourly background fields to compute the hourly increments. From these increments accumulated during the month of the simulation, we first compute the mean per instrument type (Fig.4). Note that the mean increment is an indication of the bias between the background state and the observations.

The mean increments have a different structure for the two selected spectral bands (microwave and infrared) both over sea and land. This supports the original choice of splitting the fields per spectral band. For the infrared instruments, there are similarities between the fields from the instruments on board geostationary and polar orbiting satellites, but the amplitude of the mean increment is lower for the fields from the second category. One should nevertheless be careful when comparing mean values of the two fields as the sampling is sparser from the polar orbiting satellites for which a region is observed only twice a day per instrument. The mean values are unexpectedly large for the geostationary field considering that the channels the most sensitive to the surface are not assimilated. This is likely due to an enhance sensitivity to the surface in the assimilated channels when the atmosphere is cold and/or dry.

For polar orbiting satellites only, the mean field for the microwave instruments has much higher values than for the infrared instruments both over land and over sea. The origins of this difference may be multiple and difficult to disentangle. First the model skin temperature could be a better background for the

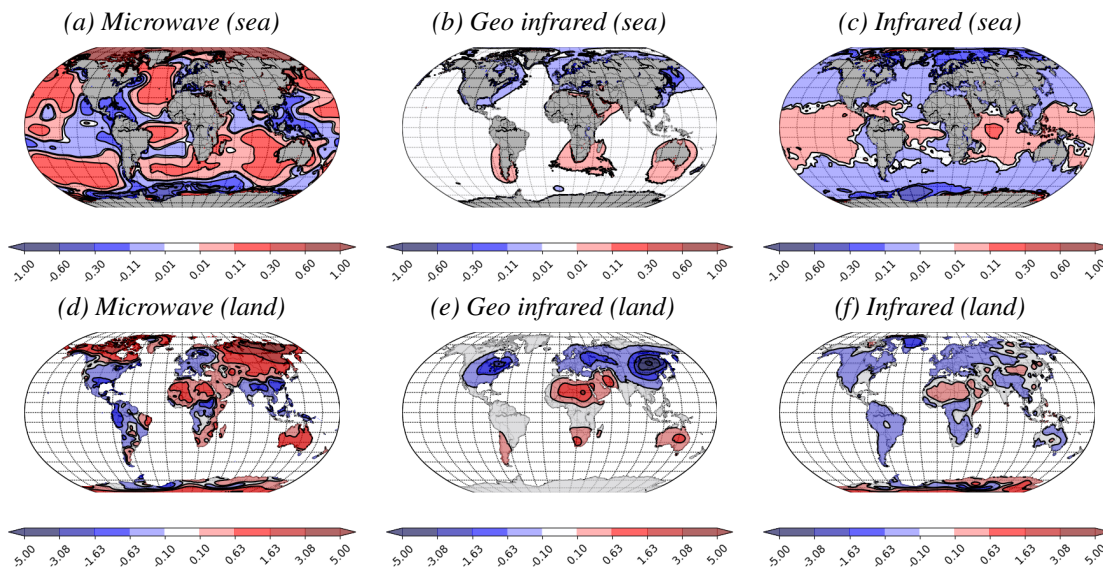


Figure 4: Mean skin temperature increment (in K) for the TOVSCV_2D reference experiment for the month of November 2019 and for the 09Z and 21Z cycles together. Top: over sea. Bottom: over land.

infrared field than for the microwave that has a deeper sensitivity to the surface. Then the mean increment for the infrared instruments could be smaller over land due to the channel selection, the channels the most sensitive to the surface being removed over land. And lastly, the cloud detection scheme rejects more low-peaking infrared channels which would affect the ability of the infrared instrument to constrain the skin temperature field. It is worth keeping in mind too that over land the emissivity is recomputed for the microwave data using the window channels. The skin temperature analysis for microwave over land depends very much on the error in this estimate of emissivity.

For all three fields, the mean increments have all lower values over ocean than over land, likely due to the lower value of the skin temperature background error standard deviation over sea compared to over land and ice and likely due to a better background state too. Over land, there are some regions where the mean increments are similar for all instrument types like North Africa, and other regions where the mean increments have opposite signs like North East Asia. Over ice, the mean increments tend to be similar in the Antarctic but tend to have opposite signs over the Arctic between the fields from the microwave and infrared instruments.

We highlight three regions to present the time variation of the increments. The first region is Australia (over land only), the second region is East Asia (over land) where the mean increment for the geostationary instruments are largest in size and have a negative sign, and the third region is the North Pacific ocean region. The geographical locations of the three regions are presented in Appendix A. For each region we compute at each hour of the day the mean value and the standard deviation for the region and over the 30 days of the simulation. This gives us the mean diurnal cycle and its standard deviation (Fig. 5).

Over Australia, the mean diurnal cycles of the three fields all suggest an increase of the skin temperature between 3 UTC and 5 UTC (mid afternoon) compared to their respective background, but with an amplitude of around 2.5 K for the microwave field, of around 1.5 K for the geostationary field and of around 0.5 K for the infrared field. The shift in time between the geostationary on one hand and the microwave and infrared on the other hand could be linked to the availability of the data around this region. Between 12 UTC and 17 UTC when both infrared and microwave data are available in the region, the infrared field

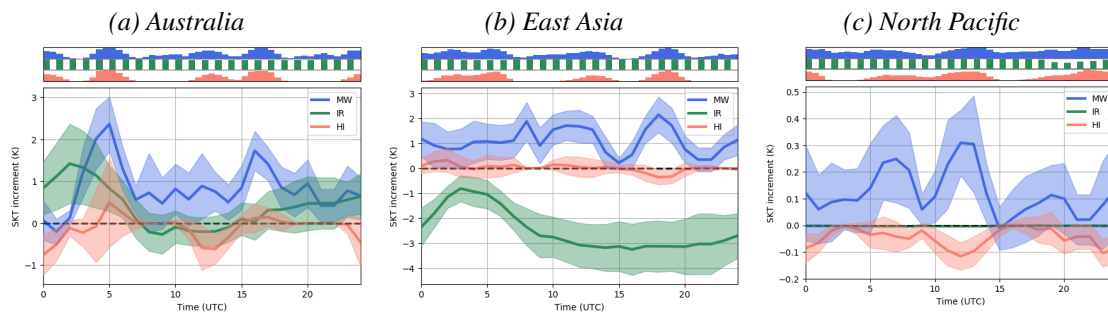


Figure 5: Skin temperature increment mean diurnal cycles (solid lines) and their standard deviation (shade) for three regions and for the three instrument types: microwave (blue), geostationary (green) and infrared (red). In the top panel, the height of the bar is proportional to the number of observations in the region for each instrument types (same color code as the bottom panel) per 30 min timeslot. The statistics are computed for November 2019. See Appendix A for the details of the three regions.

suggests a decrease of about 1 K while the microwave field suggests an increase of about 1.5 K later on and with a shift in time of 3 h. The difference in amplitude can be linked to the depth down to which each instrument is sensitive as explained before.

While the three fields produce similar increments over Australia, they differ much more over East Asia. There, the infrared field produces small increments compared to the two others. The diurnal cycle as seen by the microwave instruments suggests an increase between 1 K and 2 K of the background skin temperature. The diurnal cycle as seen by the geostationary instruments suggests a decrease up to 4 K of the background with a more pronounced variation in time of the diurnal cycle.

Over the North Pacific ocean, we have only few measurements from one geostationary instrument (GEOS-15) and the increment from the geostationary field is very small compared to the increments derived from the two other fields. From these two fields, we have a similar diurnal cycle but with an opposite sign and stronger amplitude for the microwave instruments (up to 0.3 K to be compared to -0.1 K for the infrared instruments). One can notice the sudden drop in the mean increment from the microwave field at 12 UTC due to the a gap in the availability of data over this region at that time of the day.

These three examples show some of the challenges involved in constructing a model for the time propagation of the skin temperature fields for the three instrument types we have considered. They also show we can retrieve information on the skin temperature even if our channel selections is not designed for that purpose.

4.3 Results in observation space

4.3.1 Skin temperature analysis

The background and analysis of the skin temperature for each assimilated radiance measurement that requires one are stored in the Observational DataBase (ODB, Fouilloux, 2009). Thus, for each skin temperature analysis from the TOVSCV_2D_REF experiment, we can extract the matching skin temperature analysis from the TOVSCV_0D experiment and compute the difference (TOVSCV_2D_REF-TOVSCV_0D). We select only the skin temperature analysis for the fields of view having active surface-sensitive channels. Figures 6 to 8 present the density distribution of the differences for the whole month of November 2019 for some sensors from the three types of instrument. The differences are additionally stratified

into two categories depending if the observation is over land or not.

One general characteristic among all sensors, is that for each one of them, the standard deviation of the differences is always larger over land. The values of the standard deviation are then relatively homogeneous between the sensors of the same category: around 2.25 K (1.3 K) for the microwave instruments, around 1.5 K (0.1 K) for the geostationary instruments and around 1.75 K (0.7 K) for the infrared instruments over land (sea).

For the geostationary instruments, the mean difference over land varies among the sensors with values between -0.6 K (Himawari-8) and 0.3 K (METEOSAT-11). This highlights the regional differences as the geostationary instruments sample different regions. The mean of the differences is more homogeneous among the microwave sensors and also among the infrared sensors. For the microwave instruments, the skin temperature analysis in observation space is on average larger in the TOVSCV_2D_REF experiment compared to the TOVSCV_0D by about 0.5 K over land and about 0.25 K over sea. For the infrared instruments, we have the opposite with a mean difference of about -0.3 K over land and about -0.1 K over sea.

4.3.2 Analysis fit to observations

The skin temperature analyses from the TOVSCV_0D and TOVSCV_2D_REF experiments are consistent but with a non-negligible mean and standard deviation values of the differences, especially over land. To assess the impact of these changes of the skin temperature analysis, we investigate here the difference in the overall ability of the analysis to fit the radiance observations. The assessment is based on the standard deviation of the analysis departures (analysis in observation space minus observation).

Figure 9 presents the standard deviation of the analysis departures from the two TOVSCV_0D and TOVSCV_2D_REF experiments normalised by the standard deviation of the analysis departure from the REFERENCE experiment for few instruments. Overall, the TOVSCV_0D formulation allows the analysis to have a closer fit to the radiance observations. As expected, the change in fit depends on the channel and is mostly larger for the channels sensitive to the surface. Channels less or not sensitive to the surface also benefit from the TOVSCV_0D formulation. For example, we have an improvement for all the ATMS humidity-sounding channels (18 to 22), even if channel 18 is the most surface sensitive and 22 the least one. On the other hand, we use channels 20-22 over more surfaces, whereas we reject channels 18 and 19 over some surfaces.

The TOVSCV_2D_REF experiment does also mostly have an analysis with a closer fit to radiance observations for microwave and infrared measurements but less than the TOVSCV_0D experiment and not for all channels. For example, there is an increase in the analysis fit to the ATMS humidity-sounding channels (18 to 22) and for the wavenumbers around 1050 cm^{-1} for CRIS. For the geostationary instruments, the TOVSCV_2D_REF experiment systematically increases the fit to observation.

The TOVSCV_2D_REF experiment produces a cooler/drier troposphere in the northern hemisphere and a warmer/wetter troposphere in the southern hemisphere. This makes its analysis fit to observation systematically larger for temperature and humidity profiles from radio-sondes by up to 3% (not shown) compared to the REFERENCE experiment. The changes in mean tropospheric temperatures are propagated in the stratosphere and also make its analysis not able to fit the GPS-RO observations as well as the the analysis from the two other experiments (Fig. 9d).

This behaviour suggests that we may be inappropriately aliasing atmospheric signal into the skin temperature in the TOVSCV_2D_REF experiment. This is likely a consequence of too large background error

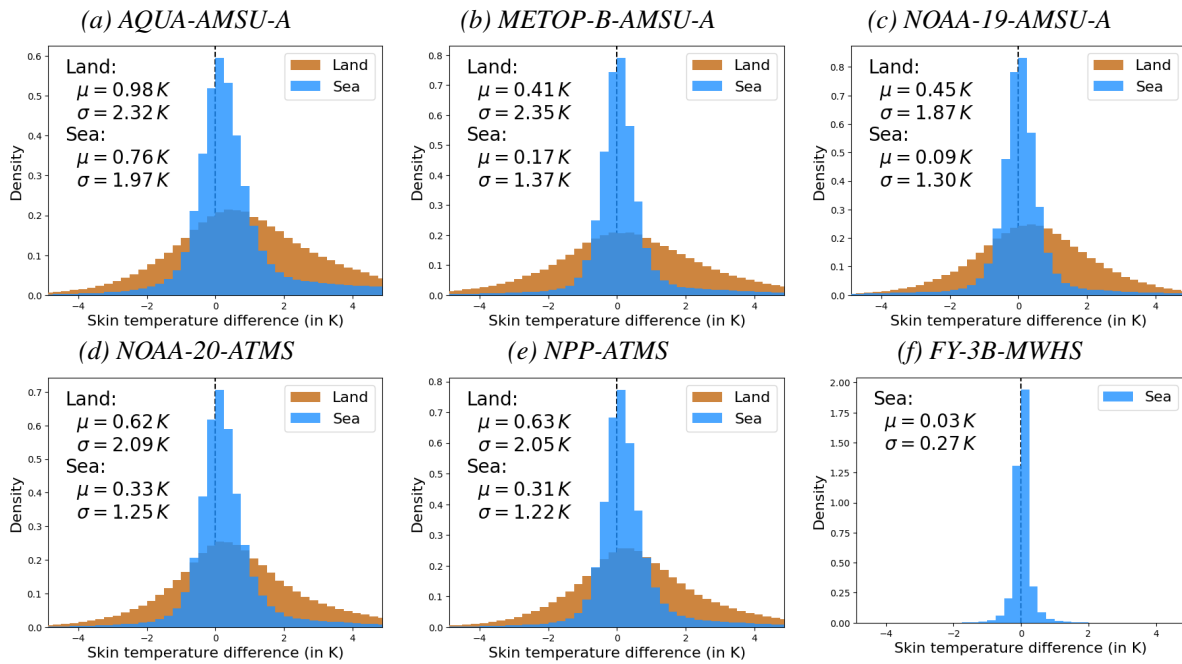


Figure 6: Distribution of the differences in observation space between the analysed skin temperature from the TOVSCV_2D_REF experiment and the analysed skin temperature from the TOVSCV_OD experiment, for some of the microwave instruments and over land (brown) and over sea (blue). The values of μ and σ are respectively the mean difference and its the standard deviation.

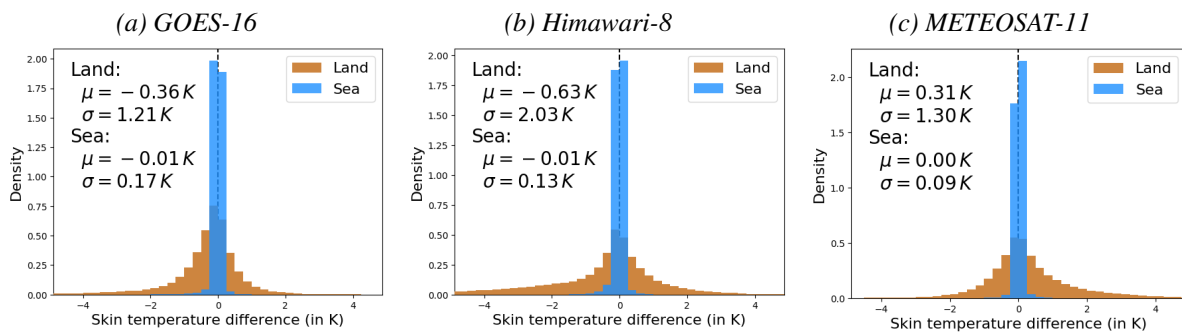


Figure 7: Same as Fig. 6 but for some geostationary infrared instruments.

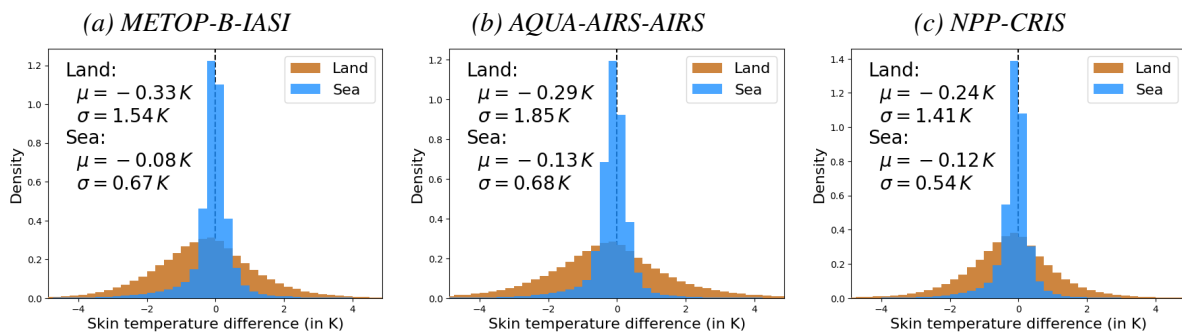


Figure 8: Same as Fig. 6 but for some hyper-spectral infrared instruments.

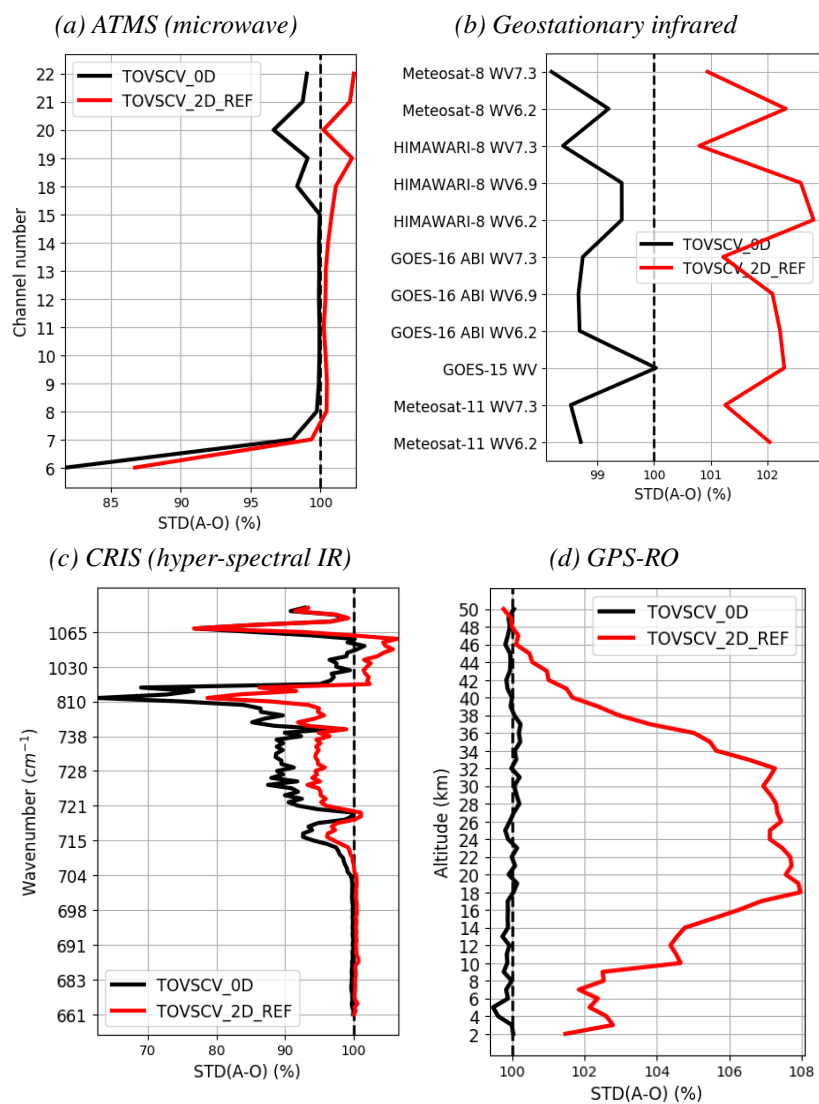


Figure 9: Standard deviation of the analysis departure (analysis minus observation) for the TOVSCV_0D (black) experiment and for for the TOVSCV_2D (red) normalised by the standard deviation of the analysis departure of the REFERENCE experiment.

standard deviations of the skin temperature fields in this experiment. The effective standard deviation is indeed higher in the TOVSCV_2D_REF experiment than in the TOVSCV_0D experiment due to the introduction of background error correlation in the former experiment (see Appendix B for more details about effective standard deviation). This makes the analysis fit to allow much larger adjustments to the skin temperature to fit the radiance observations and to allow less adjustment of other model variables, which in turn increases the analysis fit to radiance observations for channels not or less sensitive to the surface and to other observations too.

4.3.3 Variational bias correction

We discussed that the TOVSCV_2D_REF experiment produces a skin temperature analysis with a systematic instrument-dependent and surface-dependent bias compared to the TOVSCV_0D experiment. These biases influence the analysis fit to observations, and therefore could also change the analysis of the bias correction provided by VARBC.

Over the month of experiment, there are no major differences in the analysed bias correction between the two experiments (not shown). The biggest difference is found for channels 9 and 10 of AQUA. For them, the difference between the analysed bias correction remains almost constant after the first 5 days of experimentation and the value of the difference is around 0.02 K in average. The maximum local difference is found in the Arctic region with a value of 0.05 K.

At this stage of experimentation, we can assume that the TOVSCV_2D formulation has very little impact on the behaviour of the variational bias correction.

5 Sensitivity experiments

In the previous section, we showed that the TOVSCV_2D formulation produces too large increments of skin temperature when using the same skin temperature background error standard deviation as for the TOVSCV_0D formulation. We discussed that this was likely a consequence of the introduction of background error spatial correlations in the TOVSCV_2D formulation that increases the effective standard deviation. In order to test this hypothesis, we present in this section some sensitivity experiments for which we changed the values of the skin temperature background error standard deviation. We also assess the impact of changing the background error correlation length and time scales.

5.1 Experimental configuration

We carried out a set of four sensitivity experiments with the TOVSCV_2D formulation. For simplification, we omitted the TOVSCV_2D prefix in the experiment names (Tab. 4). The REF experiment is the TOVSCV_2D experiment discussed in the previous section.

In order to have a more reasonable comparison between the two TOVSCV formulations, we adjusted the background error standard deviation of the TOVSCV_2D formulation until reaching a similar analysis fit to observations for the two formulations. After some experimentation, we found we could produce a similar analysis fit to observations when the background error standard deviation was divided by a factor 3. We then ran the ERR/3 experiment using this new value of background error standard deviation. This means that we still have a single value of standard deviation per surface type (land/sea/ice) and a

Table 4: Configuration of the background errors for the sensitivity experiments with the TOVSCV_2D formulation.

Name	Standard Deviation	Spatial Correlation	Temporal Correlation
REF	Fixed	Constant (300 km)	None
ERR/3	Fixed but divided by 3	Constant (300 km)	None
EDAx2	From EDA and multiplied by 2	Constant (300 km)	None
HCOR	From EDA and multiplied by 2	From EDA (fixed)	None
TCOR	From EDA	From EDA (fixed)	From EDA (fixed)

linear interpolation in the interface between the surface types. The value of the standard deviation for each surface type is the one provided in the middle row of Tab. 1 but divided by 3.

For the next experiment, we wanted to use the skin temperature background error standard deviation as derived by the EDA. Even when divided by a factor 3, the standard deviation values of the *ERR/3* experiment are still larger than the one derived from the EDA, especially over land. We found that the analysis fit to observations was similar to the one from the *ERR/3* experiment when the standard deviation derived from the EDA were multiplied by a factor 2. The experiment *EDAx2* thus uses the skin temperature background error standard deviation as derived by the EDA but multiplied by a factor 2. Compared to the *ERR/3* experiment, here we also have a skin temperature background error standard deviation per hour as presented in section 3.

The last two experiments make use of the EDA output for the skin temperature background error spatial and temporal correlation. The *HCOR* experiment is similar to *EDAx2* but uses EDA-derived spatial error correlations. At this stage, the length-scales are not flow-dependent and are constant in time. The *TCOR* experiment includes the temporal correlation as presented in section 3. Similarly to the spatial correlation, adding the temporal correlation increases the effective variance. For this reason, we had to decrease the background error standard deviation to have similar analysis fit to observations as for the other experiments. For the *TCOR* experiment, the background error standard deviation values are the ones directly sampled from the EDA.

5.2 Impact of background error standard deviation

When decreasing the background error standard deviation, either by a factor 3 or using the value from EDA times 2, the bias in the skin temperature analysis between the TOVSCV_2D experiments and the TOVSCV_0D experiment is overall reduced (Fig. 10). Over sea, there is still a residual mean difference of about 0.1 K for the microwave instruments. For the other instruments, the difference is now negligible. Over land, there is a residual mean difference of about 0.25 K for the microwave instruments, and of less than -0.1 K for infrared instruments. The difference is consistent between all the instruments inside the same type, with the possible exceptions of AMSU-A on-board AQUA and Himawari 8 for which the difference is slightly higher.

Due to instrument problems, the three lowest-peaking channels (5-7) of AQUA AMSU-A are presently not used. This reduces the constraint of this instrument on its skin temperature analysis in the TOVSCV_0D approach. This likely affects the comparison between the two TOVSCV approaches and explains the largest differences for this particular microwave instrument compared to others.

The standard deviation of the difference in skin temperature analysis between the *ERR/3* experiment or the *EDAx2* experiment and the TOVSCV_0D experiment is also reduced compared to the TOVSCV_2D

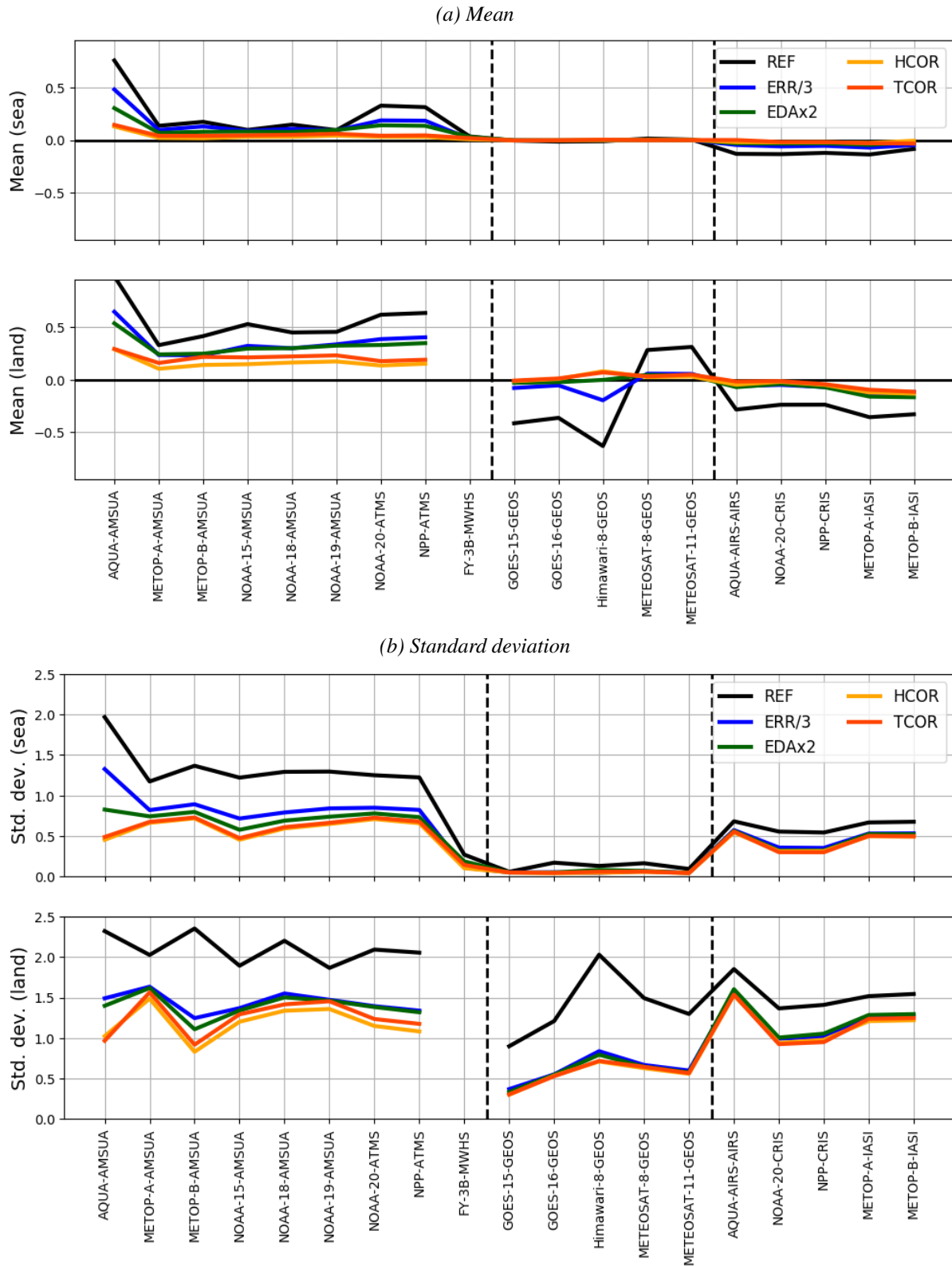


Figure 10: Statistics of the difference in skin temperature analysis between the TOVSCV_2D experiments (see legend and Tab. 4) and the TOVSCV_0D experiment for each instrument requiring a skin temperature field. (a) mean difference. (b) standard deviation of the difference. For each sub-figure, the top panel is for the statistics over sea and the bottom panel for the statistics over land. The vertical dashed lines separate the instrument types: (left) MW, (middle) IR, (right) HI.

reference experiment. With values around 0.5 K over sea, the standard deviation remains lower for the infrared instruments than for the microwave (values between 0.5 K and 0.75 K, except for AQUA). Over land, the values are more similar and between 1.0 K and 1.5 K. The values of the standard deviation for the geostationary instruments are lower and around 0.75 K.

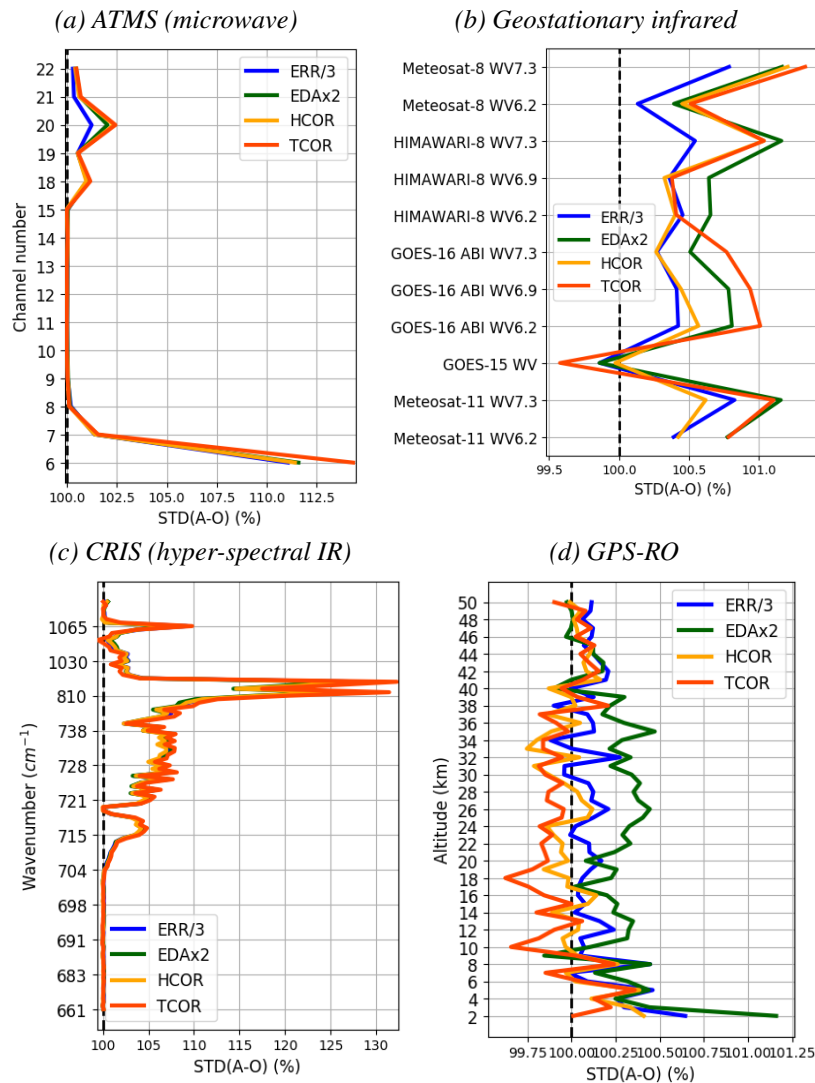


Figure 11: Standard deviation of the analysis departure (analysis minus observation) for the TOVSCV_2D sensitivity experiments normalised by the standard deviation of the analysis departure of the TOVSCV_0D experiment.

Even with the rescaling factors, the background error standard deviation of the *ERR/3* and *EDAx2* experiments are still quite different between the two experiments. Nevertheless, they are similar in terms of mean difference or standard deviation of the skin temperature analysis difference with respect to the TOVSCV_0D experiment. In terms of analysis fit to observations, there are also very few differences between the two experiments, but for the geostationary instruments and GPS-RO (Fig. 11). For these data, the *ERR/3* experiment has a more similar fit to the TOVSCV_0D experiment than the *EDAx2* experiment. The differences are nevertheless small and within 1%. This is much lower than the initial *REF* experiment and confirms the hypothesis that the background error standard deviation was too large in that experiment and that some atmospheric signal was dumped into the skin temperature increment.

The analysis fit to observation is still much larger for some channels of the microwave and infrared measurements for the two TOVSCV_2D experiments compared to the TOVSCV_0D experiment. As an example, there is a difference of more than 10% between the TOVSCV_2D sensitivity experiments and the TOVSCV_0D experiment for the channel 6 of ATMS, or a difference of more than 20% for the wavenumbers around 900 cm^{-1} for CRIS. These are therefore genuine differences between the two formulations.

5.3 Impact of background error spatial correlation

In the *HCOR* experiment, the skin temperature background error correlation length scales as derived from the EDA are space dependent and smaller over land and larger over ocean when compared to the *EDAx2* experiment for which the length scale is constant. Figures 12a to 12d illustrate the impact of using space dependent length scales on the skin temperature increment for the field associated with the infrared instruments. As expected, the increment has a smaller scale structure over land and larger scale structure over sea in the *HCOR* experiment.

The amplitude and general shape of the increments for the other instrument types and over time are similar for the two experiments. Nevertheless, the skin temperature analysis becomes closer to the skin temperature analysis from the TOVSCV_0D experiment in the *HCOR* experiment (Fig. 10), especially for the microwave instruments. The analysis fit to observations is also slightly closer to the TOVSCV_0D experiment for the geostationary instruments.

5.4 Impact of background error temporal correlation

The introduction of time correlation in the skin temperature background error in the *TCOR* experiment allows to fill the gaps in time when no radiance observation is available. This is illustrated by Figs. 12e to 12f for the skin temperature increment associated with the infrared instruments. For example, at 01Z, there are no infrared measurements over the Pacific ocean and still there is an analysis increment. This increment is the result of the propagation in time through the temporal correlation of the increment obtained at 05Z when some infrared measurements are available over that region.

Figure 13 presents the effect of the temporal correlation in the time-series of the increments over the three regions already discussed. Without the temporal correlation, the time evolution of the skin temperature increment is noisy and jumpy due to gaps in the availability of radiance observations in or around the domain. The introduction of the temporal correlation smooths the time evolution of the increment. It is interesting to see for example, that over Australia, the increment for the microwave and for the infrared instruments are similar but with the opposite sign. Over the North Pacific ocean, there is a pronounced diurnal cycle in the infrared increment that is not present in the microwave increment. These features will have to be investigated in the future to understand if we can extract information that could be used for the skin temperature model or information that could be used to design a model for the time evolution of the skin temperature fields.

The mean skin temperature analysis is very similar to the one from the TOVSCV_0D experiment for all instruments (Fig. 10). This mean value hides some regional differences though. Appendix C illustrates for example these regional differences for AMSU-A and IASI on board METOP-A. These differences will have to be studied in more details in the future to better understand the differences between the two TOVSCV approaches and better understand the benefits and weaknesses of each.

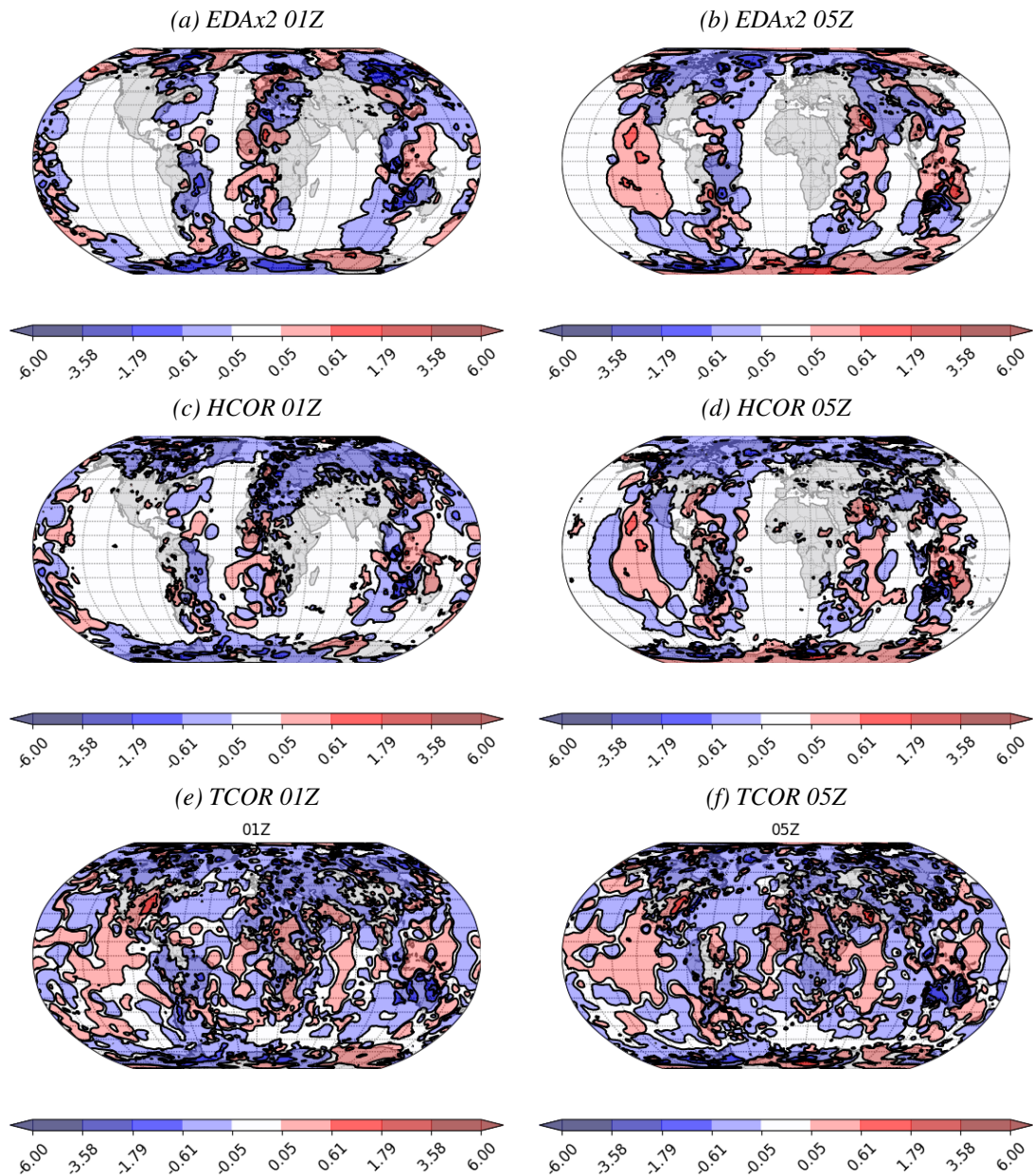


Figure 12: Examples of analysis increments of skin temperature field associated with hyper-spectral infrared instrument on 1st November 2019. Top row: increment from the EDAX2 experiment. Middle row: increment from the HCOR experiment. Bottom row: increment from the TCOR experiment. Left: increment at 01Z. Right: increment at 05Z.

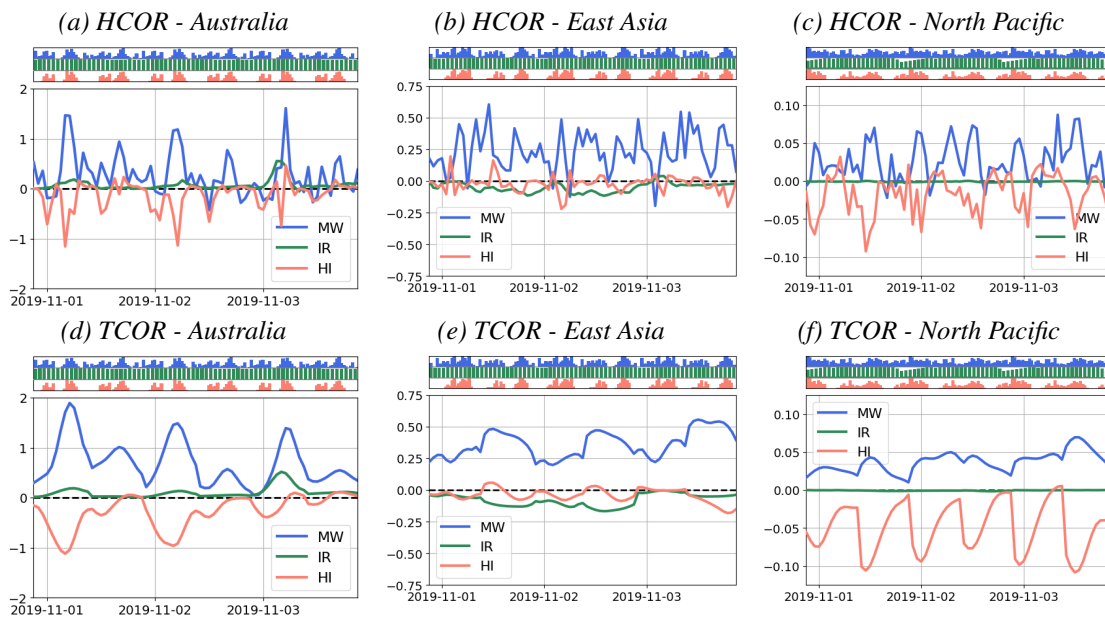


Figure 13: Time series of the skin temperature increments for the first three days of the experiments, for three regions and for the three instrument types: microwave (blue), geostationary (orange) and infrared (green). The regions are the same as for Fig. 5. Top row: HCOR experiment. Bottom row: TCOR experiment.

5.5 Forecast scores

The atmospheric analysis serves as initial condition for the short-range forecast that is used as the first guess for the next assimilation cycle. This first guess is compared to all available observations to compute the first guess departure. The standard deviation of the first guess departure gives information on the quality of the first guess. We compare here the standard deviation of the first guess departure of the TOVSCV_2D sensitivity experiments using the TOVSCV_0D experiment as a reference (Fig. 14).

For the radiance observations, the value of standard deviation of the first guess departure for the TOVSCV_2D sensitivity experiments is always within $\pm 0.5\%$ of the value of the TOVSCV_0D experiment, without significant differences, except for one particular channel of CRIS. This means that the large differences we had in the analysis fit to observations for ATMS channel 6 for example or some CRIS wavenumbers, do not have a significant impact on the first guess fit.

When comparing the TOVSCV_2D sensitivity experiments, there is not an experiment significantly better than the other. Comparing them to the TOVSCV_0D experiment, there is not a clear improvement or degradation. Yet, the HCOR and TCOR experiment seems to perform slightly better than the other.

One month of simulation is not enough for having robust statistics of the forecast scores of one experiment compared to another one. We decided to run the TCOR experiment for another 3 months, together with the TOVSCV_0D and REFERENCE experiments. Overall, the TCOR experiment performs similarly to the TOVSCV_0D experiment and they are both significantly better than the REFERENCE experiment up to day 3 to 5 (not shown). We noticed two main differences between the TCOR and the TOVSCV_0D experiments. First, the TOVSCV_0D experiment is cooler at the surface in the polar regions which makes it slightly better than the TCOR experiment when compared to observations (Fig. 15, left panel). We believe that the difference comes from the disparity of the skin temperature background error standard deviation values over sea-ice. In the TOVSCV_0D experiment their values are 7.5 times

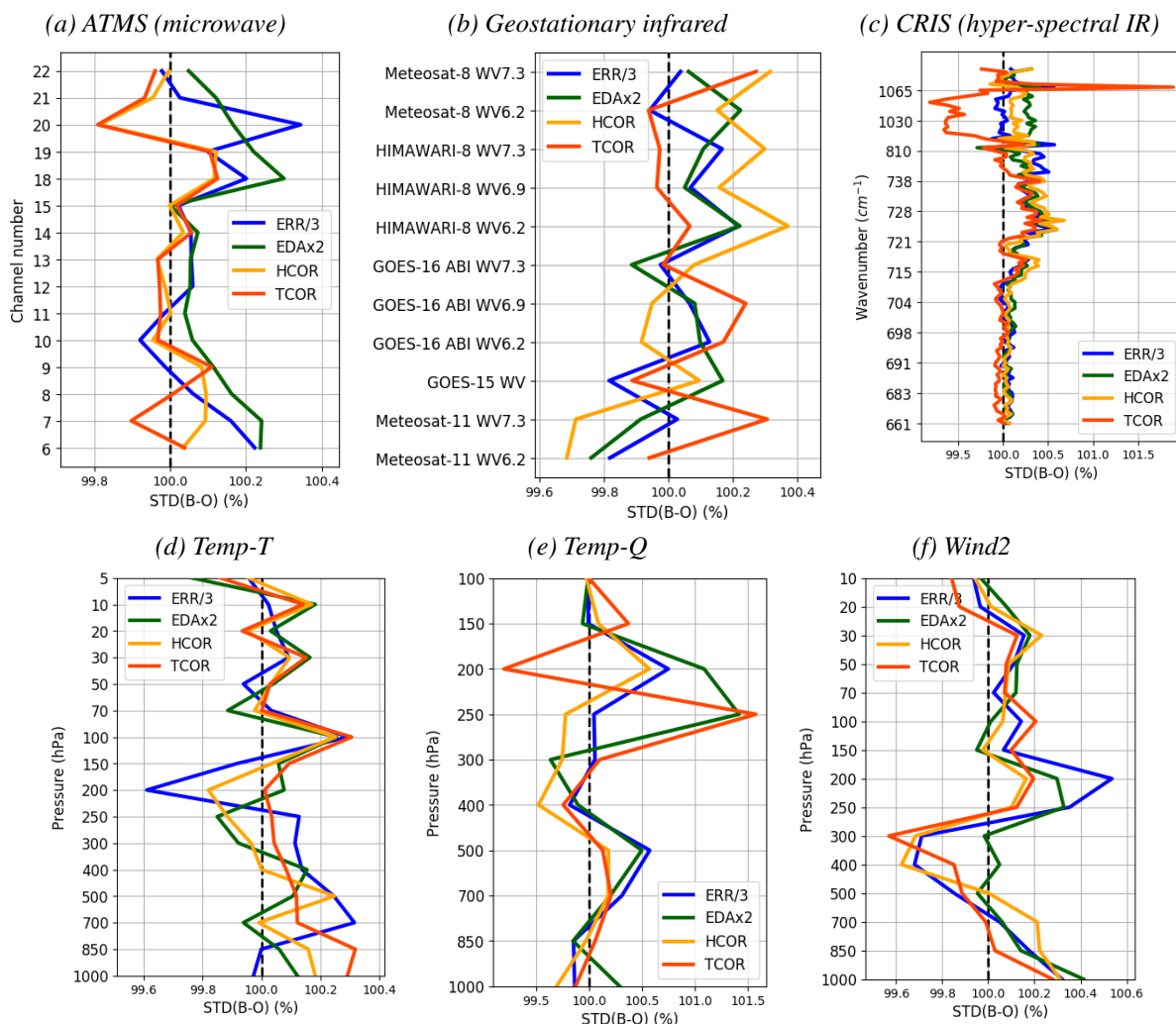


Figure 14: Standard deviation of the first guess departure (first guess minus observation) for the TOVSCV_2D sensitivity experiments normalised by the standard deviation of the analysis departure of the TOVSCV_0D experiment.

larger over sea-ice than over sea, while they are only 2 times larger in the *TCOR* experiment. Note that the sea-ice is currently not perturbed in the EDA. The second difference is the 2m dew point over the Tropics where the *TOVSCV_0D* experiment is drier. This makes it significantly worse than the *TCOR* experiment when compared to observations (Fig. 15, right panel). This needs to be further investigated but the difference in 2m dew point between the two experiments is large over North Africa. There, the correlation length scale of the skin temperature background error can be larger than 150 km and the correlation time scale larger than 1 h. The *TCOR* experiment then adds much more constraint on the skin temperature analysis from the neighbouring observations than the *TOVSCV_0D* experiment and this seems beneficial.

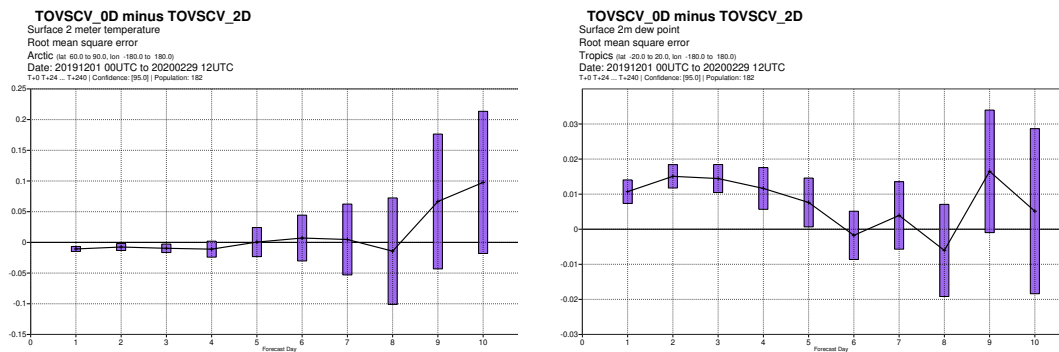


Figure 15: Normalised difference in root mean square error of the forecast against observation (black line) and its standard deviation (purple error bars), between the *TOVSCV_0D* and *TCOR* experiments for 2m temperature over Arctic (left) and 2m dew point over the Tropics (right). A positive value means that the *TCOR* experiment is better. The statistics are computed over the period from 1 December 2019 to 29 February 2020.

6 Conclusion

The vertical sensitivity of a radiance observation to the various layers of the atmosphere depends on the frequency of the measurement. Assimilating radiance observations in the IFS at various frequencies therefore provides information on the atmospheric variables on diverse atmospheric layers. Some of the assimilated frequencies makes the clear-sky radiance sensitive to the surface variables, and to the skin temperature in particular. In that case, during the assimilation process, the skin temperature has to be optimised together with all the atmospheric variables in order to produce a simulated radiance that fits in an optimal manner the observed radiance.

In the IFS, the atmospheric analysis and the surface analysis are computed separately for each outer loop. This makes it impossible to have a skin temperature analysis field in the atmospheric 4D-Var using the surface sensitive radiance observations. Instead, the atmospheric 4D-Var control vector is extended with a set of skin temperature values defined in observation space for each field of view. This is known as TOVS control variable (or *TOVSCV*) and we refer to it as *TOVSCV_0D* as each skin temperature value is optimised individually. This approach is sub-optimal and could be improved by constraining the skin temperature with all available radiance observations as it is the case for the atmospheric variables. Indeed, without spatial nor temporal constraint, the skin temperature could be adjusted to compensate

for a number of artifacts not related to skin temperature (e.g., issues with the cloud screening).

To assess if it would be beneficial for the radiance assimilation to constrain better the skin temperature, we developed a new formulation of TOVSCV that we refer to as TOVSCV_2D. For this new method, a set of two-dimensional skin temperature fields defined in model space are added to the control vector in the IFS. These fields are divided into three categories corresponding to two separate spectral bands (microwave and infrared) and two different viewing geometries (geostationary and polar) for the infrared band. For each category, we also introduced hourly fields.

The TOVSCV_2D formulation adds more constraint on the skin temperature used to assimilate the clear-sky radiance observation. We saw that including skin temperature background error correlations in the TOVSCV_2D formulation results in an increase of the effective standard deviation. A direct comparison of the TOVSCV_0D and TOVSCV_2D approaches using the same standard deviation for the skin temperature is therefore inappropriate as we discovered when comparing them with one-month experiments covering November 2019.

We divided the standard deviation of the skin temperature background errors by a factor 3 in an experiment using the TOVSCV_2D approach and we obtained a more similar skin temperature analysis between the two approaches. Yet, the TOVSCV_2D produces on average a skin temperature slightly warmer for the microwave instruments between 0.3 K to 0.6 K over land. Elsewhere and for the other instruments, the mean difference is mainly under 0.1 K. Most of the values for the standard deviation of the difference are between 0.25 K and 1.5 K, and they are the largest over land. These values are smaller than the uncertainty given to the skin temperature in the TOVSCV_0D method, but are larger than the uncertainty computed from the EDA. This means that the TOVSCV_2D makes very little difference on average to the skin temperature analysis used in the radiance observation operator. This also means that the difference in skin temperature analysis between the two methods may be locally significant in space and time.

Due to the additional constraint on the skin temperature in the TOVSCV_2D method, the analysis fit to radiance observations remains larger than for the TOVSCV_0D method. This has no negative impact on the quality of the first-guess as suggested by the first-guess fit to observations which is not significantly different between the two methods. This gave us confidence in the TOVSCV_2D method and we then wanted to determine if it could be further improved. We thus studied its sensitivity to the background errors of the added skin temperature fields. We made use of the EDA to compute the hourly background error standard deviation and to create a spatially dependent correlation length-scale and time-scale. We ran a set of experiments with the TOVSCV_2D formulation and various configurations over the same period of November 2019. The experiments are not significantly different, but the configuration using all the background error information derived from the EDA seems to be better than the others.

The purpose of this study was to present the TOVSCV_2D method and implementation, and assess the possible advantages compared to the current implementation. So far, the experimentation over one month shows that on average, there are some significant differences in the skin temperature field used for the assimilation of the radiance data, but no significant differences in terms of forecast scores. An experimentation over a longer period of four months for one configuration of the TOVSCV_2D method showed that this method has some potential to have a positive impact on the forecast scores.

The availability of a realistic and temporally and spatially consistent analysis of skin temperature can also be seen as an attractive by-product of the new method. These skin temperature analysis fields can drive further improvements in the estimation of physically connected fields (e.g., sea surface temperature, land surface temperature). Before, one has to be careful of the link between emissivity error and skin temperature error and of the fact that the emissivity is estimated using the window channels for the

microwave data over land.

The results presented in this study give enough confidence in the TOVSCV_2D method to further extend the experimentation and to further revisit the hypotheses behind the TOVSCV_2D method. The first hypothesis is that the skin temperature background fields are unbiased. In most of the sensitivity experiments the values of the monthly mean increment are mostly lower than 0.5 K except for the microwave skin temperature field for which the values can be larger than 1 K over ice and over land at latitudes above $50^{\circ}N$. These values are too large compared to the assumed background error standard deviation for these fields to neglect the bias. The background fields are currently the model skin temperature which means that the contribution of the sub-surface is not accounted for when the channel sensitivity goes deeper than the surface skin. This likely explains part of the biases and this should be further investigated to understand if the skin temperature background field for each instrument could be better modelled from the model skin temperature background. Another solution would be to correct the biases within the assimilation cycle using the weak constraint formulation currently used for the model error (Trémolet, 2006).

Similarly, if the background for each skin temperature field could be different to account for the specific sub-surface contribution of each instrument type, the background errors could also be different for each field. Unfortunately, since we do not have a model to propagate in time the skin temperature fields, we can not directly rely on the EDA to estimate the background errors of these fields. Building such a model is among the main priorities for the development of the TOVSCV_2D method and will make use of knowledge accumulated in the skin temperature analysis.

In the meantime, we can already make a better use of the EDA. In this document the skin temperature background error correlations are static. They should become more flow dependent to account for example for the changes in the sea-ice, the change in vegetation over land or the change in the gyres position over oceans. In the future, we should also envisage that each skin temperature field would have its own background error correlations.

Another hypothesis was to consider three separate skin temperature fields. This can be further refined as different channels within a category can have a difference sensitivity to the surface. For instance, low frequency channels are sensitive to a deeper surface layer than high frequency channels for the microwave instruments. For example, we could separate for ATMS the channels 6-9 (50 GHz) to the channels 18-22 (183 GHz).

Finally, our channel selections or quality control are currently designed to give the best possible forecast scores and not to have the best possible skin temperature analysis. With the TOVSCV_2D method, we may be able to add more channels that are sensitive to the surface and that were problematic to add before because of this sensitivity. Moreover, our quality control tends to reject a significant portion of microwave data over deserts or snow-covered regions because of too large biases. If we can improve our skin temperature background field, we may be able to reduce these biases and increase the number of assimilated radiance.

References

- Bonavita, M., Isaksen, L., and Hólm, E. (2012). On the use of EDA background error variances in the ECMWF 4D-Var. *Q.J.R. Meteorol. Soc.*, 138(667):1540–1559.
- Bormann, N., Lupu, C., Geer, A. J., Lawrence, H., Weston, P., and English, S. (2017). Assessment of

- the forecast impact of surface-sensitive microwave radiances over land and sea-ice. *ECMWF Technical Memoranda*, Technical Memorandum No. 804.
- Browne, P., de Rosnay, P., Zuo, H., Bennett, A., and Dawson, A. (2019). Weakly Coupled Ocean-Atmosphere Data Assimilation in the ECMWF NWP System. *Remote Sensing*, 11(3):234.
- Collard, A. (2008). Assimilation of AIRS and IASI at ECMWF. In *Seminar on Recent developments in the use of satellite observations in numerical weather prediction, 3-7 September 2007*, pages 127–150, ECMWF, Shinfield Park, Reading.
- Collard, A. D. (2007). Selection of IASI channels for use in numerical weather prediction. *Q.J.R. Meteorol. Soc.*, 133(629):1977–1991.
- Courtier, P., Thépaut, J.-N., and Hollingsworth, A. (1994). A strategy for operational implementation of 4D-Var, using an incremental approach. *Q.J.R. Meteorol. Soc.*, 120:1367–1388.
- de Rosnay, P., Balsamo, G., Albergel, C., Muñoz Sabater, J., and Isaksen, L. (2014). Initialisation of Land Surface Variables for Numerical Weather Prediction. *Surv. Geophys.*, 35:607–621.
- Dee, D. (2004). Variational bias correction of radiance data in the ECMWF system. In *ECMWF Workshop on Assimilation of High Spectral Resolution Sounders in NWP*, ECMWF, Shinfield Park, Reading.
- ECMWF (2019). Part I : Observations. *IFS Documentation*, IFS Documentation CY46R1.
- English, S. and Hewison, T. (1998). A fast generic millimetre-wave emissivity model. *Proceedings of SPIE - The International Society for Optical Engineering*, 3503.
- Eresmaa, R., Letertre-Danczak, J., Lupu, C., Bormann, N., and McNally, A. P. (2017). The assimilation of Cross-track Infrared Sounder radiances at ECMWF. *Q.J.R. Meteorol. Soc.*, 143(709):3177–3188.
- Eyre, J., Kelly, G., McNally, A., and Andersson, E. (1992). Assimilation of TOVS radiance information through one-dimensional variational analysis. *ECMWF Technical Memoranda*, Technical Memorandum No. 187.
- Fisher, M. and Andersson, E. (2001). Developments in 4D-Var and Kalman Filtering. *ECMWF Technical Memoranda*, Technical Memorandum No. 347.
- Fouilloux, A. (2009). ODB (Observational DataBase) and its usage at ECMWF. In *Twelfth Workshop on Meteorological Operational Systems, 2-6 November 2009*, pages 86–90, Shinfield Park, Reading. ECMWF.
- Gentemann, C. L., Minnett, P. J., Le Borgne, P., and Merchant, C. J. (2008). Multi-satellite measurements of large diurnal warming events. *Geophysical Research Letters*, 35(22).
- Karbou, F., Gérard, E., and Rabier, F. (2006). Microwave land emissivity and skin temperature for AMSU-A and -B assimilation over land. *Q.J.R. Meteorol. Soc.*, 132(620):2333–2355.
- Kazumori, M. and English, S. J. (2015). Use of the ocean surface wind direction signal in microwave radiance assimilation. *Q.J.R. Meteorol. Soc.*, 141(689):1354–1375.
- Matricardi, M., Chevallier, F., Kelly, G., and Thépaut, J.-N. (2004). An improved general fast radiative transfer model for the assimilation of radiance observations. *Q.J.R. Meteorol. Soc.*, 130(596):153–173.

- McNally, A. (2015). The impact of satellite data on NWP. In *Seminar on Use of Satellite Observations in Numerical Weather Prediction, 8-12 September 2014*, ECMWF, Shinfield Park, Reading.
- McNally, A. P. (2009). The direct assimilation of cloud-affected satellite infrared radiances in the ECMWF 4D-Var. *Q.J.R. Meteorol. Soc.*, 135(642):1214–1229.
- Ménétrier, B. and Auligné, T. (2015). Optimized localization and hybridization to filter ensemble-based covariances. *Mon. Weather. Rev.*, 143(10):3931–3947.
- Pinker, R., Sun, D., Miller, M., and Robinson, G. (2007). Diurnal cycle of land surface temperature in a desert encroachment zone as observed from satellites. *Geophysical Research Letters*, 34.
- Prigent, C., Rossow, W. B., Matthews, E., and Marticorena, B. (1999). Microwave radiometric signatures of different surface types in deserts. *Journal of Geophysical Research: Atmospheres*, 104(D10):12147–12158.
- Rabier, F., Järvinen, H., Klinker, E., Mahfouf, J.-F., and Simmons, A. (2000). The ECMWF operational implementation of four-dimensional variational assimilation. I: Experimental results with simplified physics. *Q.J.R. Meteorol. Soc.*, 126(564):1143–1170.
- Rodgers, C. D. (2000). *Inverse Methods for Atmospheric Sounding*. World Scientific.
- Saunders, R., Hocking, J., Turner, E., Rayer, P., Rundle, D., Brunel, P., Vidot, J., Roquet, P., Matricardi, M., Geer, A., Bormann, N., and Lupu, C. (2018). An update on the RTTOV fast radiative transfer model (currently at version 12). *Geosci. Model Dev.*, 11(7):2717–2737.
- Trémolet, Y. (2006). Accounting for an imperfect model in 4D-Var. *Q.J.R. Meteorol. Soc.*, 132(621):2483–2504.

Appendix A Regions of interest

Figure A.1 presents three regions of interest discussed in the document. The first region is Australia over land. The second region is East Asia defined as land within the box determined by the coordinates of its top left corner ($60^{\circ}N, 100^{\circ}E$) and of its bottom right corner ($30^{\circ}N, 140^{\circ}E$). The last region is the North Pacific Ocean defined as ocean within the box determined by the coordinates of its top left corner ($58.2^{\circ}N, 180^{\circ}W$) and of its bottom right corner ($20^{\circ}N, 100^{\circ}W$).

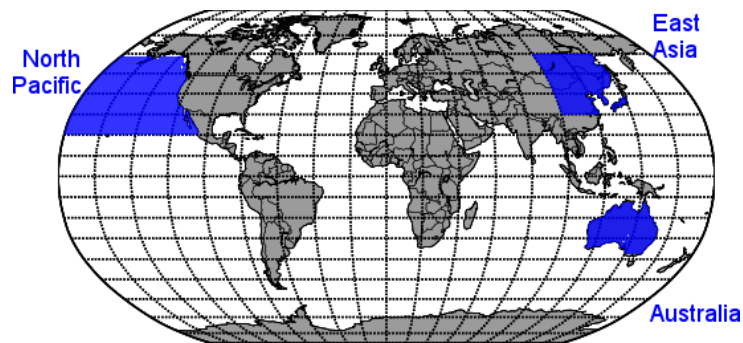


Figure A.1: Selection of regions of interest (blue areas). Top left: North Pacific (over ocean only). Top right: East Asia (over land only). Bottom right: Australia (over land only)

Appendix B Effective variance

We discussed in section 4.3.2 that using background error correlation in the TOVSCV_2D approach results in having larger effective background error variances than the TOVSCV_0D approach and therefore larger increment. This appendix aims at illustrating this effect with a simple toy model of a control vector with only two components and an observation operator being the identity. We define the background error covariance matrix as

$$\mathbf{B} = \sigma_b^2 \begin{pmatrix} 1 & \rho \\ \rho & 1 \end{pmatrix}, \quad (22)$$

where σ_b^2 is the background error variance and ρ the background error correlation. We assume here that the variances are the same for the two components of the control vector.

As the observation operator is identity, the observation error covariance matrix \mathbf{R} has the same dimension as \mathbf{B} and we assume here a diagonal matrix with the same observation error variance σ_o^2 for the two observations,

$$\mathbf{R} = \sigma_o^2 \begin{pmatrix} 1 & 0 \\ 0 & 1 \end{pmatrix}. \quad (23)$$

In this simple example, we can explicitly compute the expression of the analysis increment $\delta \mathbf{x}^a$ of the best linear unbiased estimator

$$\delta \mathbf{x}^a = \mathbf{B} (\mathbf{B} + \mathbf{R})^{-1} (\mathbf{y}^o - \mathbf{x}^b), \quad (24)$$

where \mathbf{y}^o is the observation vector and \mathbf{x}^b the background. Let us define the innovation vector,

$$\mathbf{d}^a = \mathbf{y}^o - \mathbf{x}^b = \begin{pmatrix} d_1 \\ d_2 \end{pmatrix}. \quad (25)$$

Then the analysis increment is

$$\delta \mathbf{x}^a = \frac{1}{(1+r^2)^2 - \rho^2} \begin{pmatrix} 1+r^2 - \rho^2 & \rho r^2 \\ \rho r^2 & 1+r^2 - \rho^2 \end{pmatrix} \mathbf{d}, \quad (26)$$

where $r = \frac{\sigma_o}{\sigma_b}$. let us split the analysis increment into its two components,

$$\begin{cases} \delta x_1 = \frac{(1+r^2 - \rho^2) d_1 + \rho r^2 d_2}{(1+r^2)^2 - \rho^2} \\ \delta x_2 = \frac{(1+r^2 - \rho^2) d_2 + \rho r^2 d_1}{(1+r^2)^2 - \rho^2} \end{cases}. \quad (27)$$

The increment is in particular a function of two components of the innovation vector and of the correlation ρ . If $\rho = 0$, then the first component of the analysis increment is for example a function of only the first component of the innovation vector,

$$\delta x_1 = \frac{1}{(1+r^2)} d_1. \quad (28)$$

We call effective background error variance $\tilde{\sigma}_b^2$ the background error variance that would need to be used to have the same increment without correlation, i. e. for the first component if the analysis increment

$$\frac{1}{(1+\tilde{r}^2)} d_1 = \frac{1}{(1+r^2)^2 - \rho^2} ((1+r^2 - \rho^2) d_1 + \rho r^2 d_2) \quad (29)$$

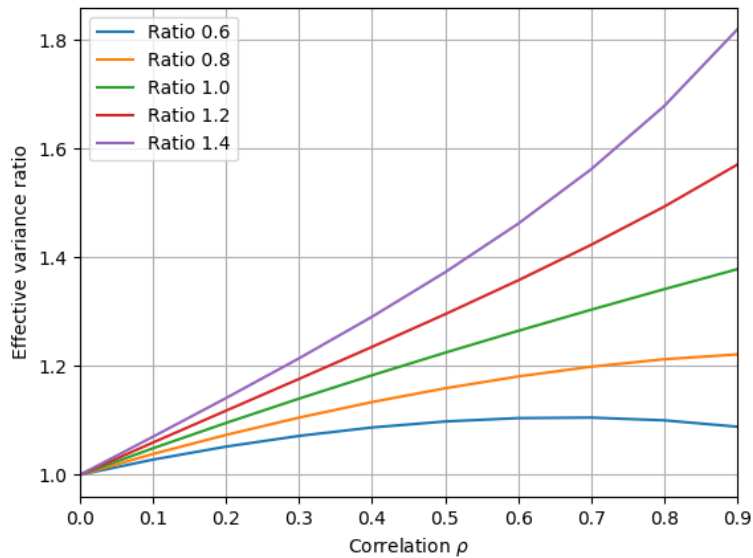


Figure B.2: Example of effective background error variance as a function of background error correlation. The different lines represent different ratio of d_2/d_1 (see text for details).

where $\tilde{r} = \frac{\sigma_o}{\sigma_b}$. To illustrate this equation, we have computed the ratio between $\tilde{\sigma}_b^2$ and σ_b^2 for a case where $\sigma_o = \sigma_b^2$ and for different value of the ratio d_2/d_1 (Fig. B.2).

In this example, if the innovations are the same and the background error correlation is 0.5, then the effective variance is about 1.2 times the background variance. This means that using a background error correlation in that case would be similar than an increase of the background error variance of about 20%. In other words, the increment for the TOVSCV_2D approach would be similar to an increment obtained with the TOVSCV_0D approach but with a background error variance increased by about 20%.

The effective variance ratio increases with the correlation ρ . There is also a significant dependence on the ratio between the two components of the innovation vector. This simple example justifies why we need to decrease the background error variance in the TOVSCV_2D approach to have similar increment as the TOVSCV_0D approach. It also shows that the amount by which we should decrease the variance is dependent of the background error correlation, the innovation and the observation background error variance too.

Appendix C Skin temperature analysis of the TCOR experiment

The TOVSCV_2D formulation gives access to two dimensional fields of the skin temperature analysis for each instrument type. By construction, we do not have such fields in the TOVSCV_0D formulation. So, to compute the regional differences between the two approaches, we compute the mean skin temperature analysis of each experiment on a $4^\circ \times 4^\circ$ grid, by averaging for each grid cell all the individual skin temperature analysis from the ODB that are present within this cell during the month of the simulation. The mean skin temperature analysis is computed over land and over sea and computed for the 09Z and the 21Z analysis cycles.

Figure C.3 presents the difference between the mean skin temperature analysis from the *TCOR* experiment and the TOVSCV_0D experiment, using an additional Gaussian filter to smooth the fields.

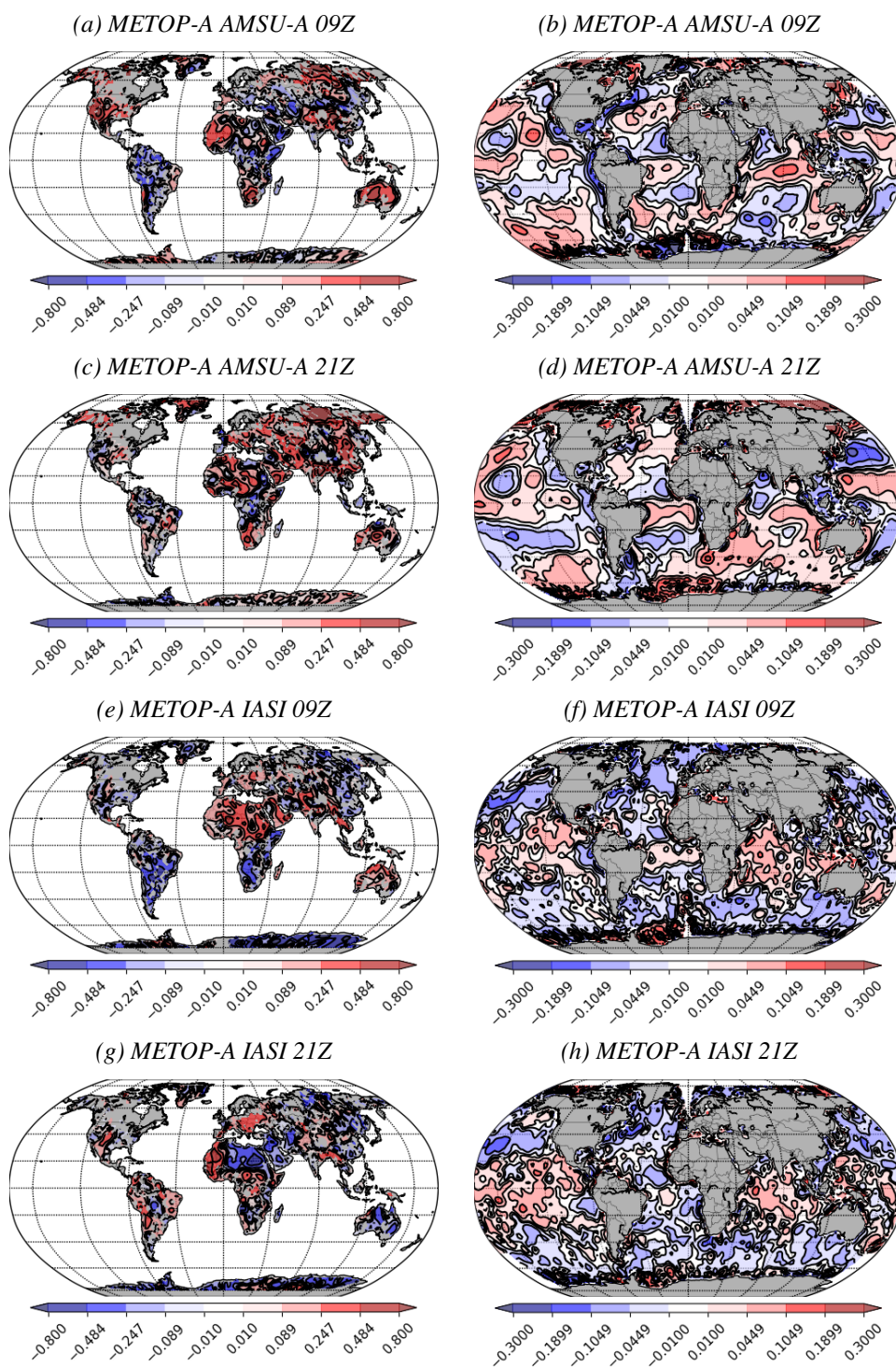


Figure C.3: Differences between the mean skin temperature analysis (in K) from the TCOR experiment and from the TOVSCV_0D experiment for METOP-A AMSU-A (a to d) and for METOP-A IASI (e to h). Left: over land. Right: over sea. For each instrument, we have the 09Z and the 21Z analysis cycles.